A Numerical and Experimental Investigation of Ram Accelerator Mixture Transition Phenomena

by

Jacqueline Auzias de Turenne

A thesis submitted in partial fulfillment
of the requirements for the degree of

Master of Science in Aeronautics and Astronautics

University of Washington

1992

Approved by _____
(Chairperson of Supervisory Committee)

Program Authorized
to Offer Degree _____

Date _____

University of Washington

Abstract

A Numerical and Experimental Investigation of
Ram Accelerator Mixture Transition Phonomena

by Jacqueline Auzias de Turenne

Chairperson of the Supervisory Committee: Professor Adam P. Bruckner
Department of Aeronautics
and Astronautics

The ram accelerator is a propulsion device both conceived and developed at the University of Washington. Its operation is governed by gasdynamic principles similar to those of an airbreathing ramjet. A projectile resembling the centerbody of a ramjet travels through a stationary tube containing a premixed gaseous fuel and oxidizer combination. The projectile carries no onboard propellant, and the combustion process travels with the projectile. The resulting pressure distribution creates forward thrust. Consequently, the ram accelerator accelerates through the tube. By subdividing the tube into distinct stages, gas mixtures with different pressures, chemical compositions, acoustic velocities, and energy densities can be used to tailor ram accelerator performance in different velocity ranges. This thesis investigates the phenomena associated with gas mixture transition between stages. An axisymmetric numerical model simulates the effects of mixture transition on the oblique shock structure, and the computational results are compared to experimental data.

TABLE OF CONTENTS

LIST OF FIGURES

Number

LIST OF TABLES

Number

NOMENCLATURE

ARABIC

c	acoustic speed
e	energy per unit volume
F	flux vector
G	flux vector
H	vector containing axisymmetric terms in Cartesian coordinates
J	Jacobian
L	characteristic length
p	pressure
Q	vector containing conservation variables in Cartesian coordinates
Δq	heat per unit volume
r	radial dimension
S	source vector
t	time in physical plane
U	contravariant velocity
u	horizontal velocity component
V	contravariant velocity
V_n	normal velocity component
V_t	tangent velocity component
v	vertical velocity component
x	horizontal coordinate
y	vertical coordinate
z	acoustic impedance

GREEK

γ ratio of specific heats

ε internal energy

ε_d dissipation coefficient

η curvilinear coordinate normal to surface

ξ curvilinear coordinate tangent to surface

ρ density

τ time in computational plane

SUPERSCRIPTS

$()^*$ dimensionless quantity

$()^n$ iteration number

$(\overline{})$ predicted value

$(\sim)$ generalized coordinate

SUBSCRIPTS

$()_i$ component in the ith direction

$()_j$ position index along ξ

$()_k$ position index along η

$()_\infty$ freestream value

ACKNOWLEDGEMENTS

I. INTRODUCTION

The ram accelerator is a chemically driven propulsion device developed at the University of Washington. It uses thermodynamic principles similar to those of an airbreathing ramjet to accelerate projectiles to high velocities [1,2,3]. An airbreathing ramjet engine is shown in Fig. 1 and compared with the ram accelerator, which is shown in Fig. 2. As the ramjet travels supersonically through the atmosphere, the air flow is compressed through a system of oblique shocks. The fuel is injected into the flow behind the centerbody and burned subsonically. An area contraction mechanically chokes the flow behind the combustion zone. The heat released during combustion and the area contraction stabilize a normal shock on the centerbody. The expanding flow through the exit nozzle produces thrust.

In the ram accelerator, the outer cowling of the ramjet is replaced by a stationary tube which contains a premixed combustible gas mixture at high pressure. A projectile, analogous to the centerbody of the ramjet, travels supersonically through this tube. The shock system which develops and the resultant pressure field accelerate the projectile as it travels down the tube. A combustion zone follows the projectile through the tube, thermally choking the flow behind the projectile and supporting a normal shock along the projectile body. All prerequisites for combustion are provided within the gas mixtures, and, unlike the ramjet, the projectile does not carry any onboard propellant or oxidizer. The ram accelerator is fully scaleable in size, and its many potential applications include a surface-to-orbit launch method for

acceleration-insensitive payloads [4,5], a hypersonic test facility [6,7,8], and a tool for hypervelocity impact studies [7].

Several modes of ram accelerator propulsion span the velocity range from subdetonative velocities, or velocities below the Chapman-Jouguet (C-J) detonation speed of the gas mixture, to superdetonative velocities, or velocities above the C-J speed [3,9]. These operating modes utilize both subsonic and supersonic combustion. The majority of experimental and theoretical work, however, has emphasized the thermally choked subsonic combustion mode. During thermally choked operation, projectiles have accelerated to speeds up to 2700 m/sec.

By subdividing the tube into stages, or distinct segments separated by thin diaphragms, gas mixtures with different pressures and chemical compositions can be used to tailor ram accelerator performance in different velocity ranges. Optimum performance over a wide range of Mach numbers is achieved with multiple stages, and the current experimental facility can accommodate up to four different gas mixtures. Transitions between successive stages have a significant effect on the flow field around the projectile. Consequently, the mixture transition process is a critical component of ram accelerator operation.

This thesis is directed toward the ram accelerator transition process between different gas mixtures and focuses specifically on the oblique shock structure generated by the projectile nose cone. A numerical code models the effects of mixture transition on the oblique shock structure, and the computational results are compared with experimental data. First of all, the

experimental apparatus is described, followed by a discussion of ram accelerator propulsion modes. The mathematical principles for the numerical solution of the Euler equations are then introduced, along with some details of the two dimensional MacCormack predictor/corrector method used to computationally model the ram accelerator's oblique shock system. Numerical and experimental results are then presented and compared, followed by the final concluding remarks.

OUTER COWLING

FUEL INJECTION

MECHANICAL CHOKING

M > 1

CENTERBODY

$M < 1$

COMBUSTION

$M = 1$

OBLIQUE SHOCK

NORMAL SHOCK

Fig. 1: Airbreathing Ramjet.

STATIONARY TUBE

NORMAL SHOCK

THERMAL CHOKING

M > 1

$M < 1$

PROJECTILE

COMBUSTION

$M = 1$

PREMIXED FUEL / OXIDIZER

OBLIQUE SHOCK
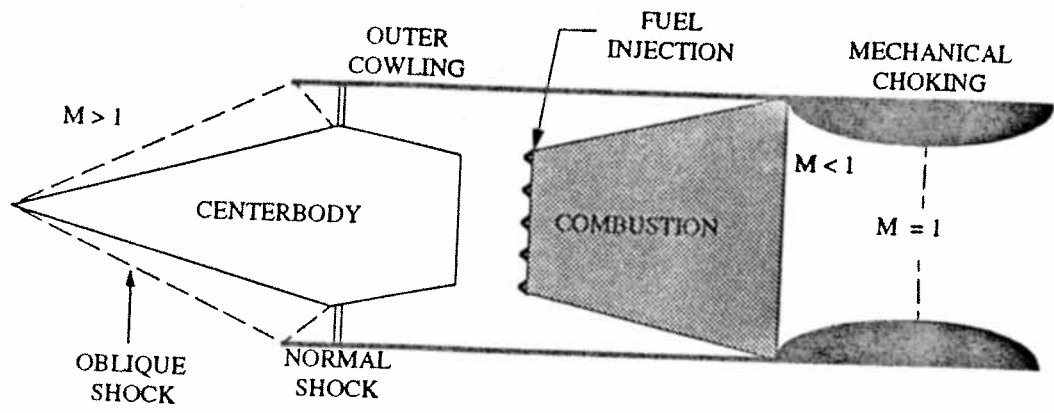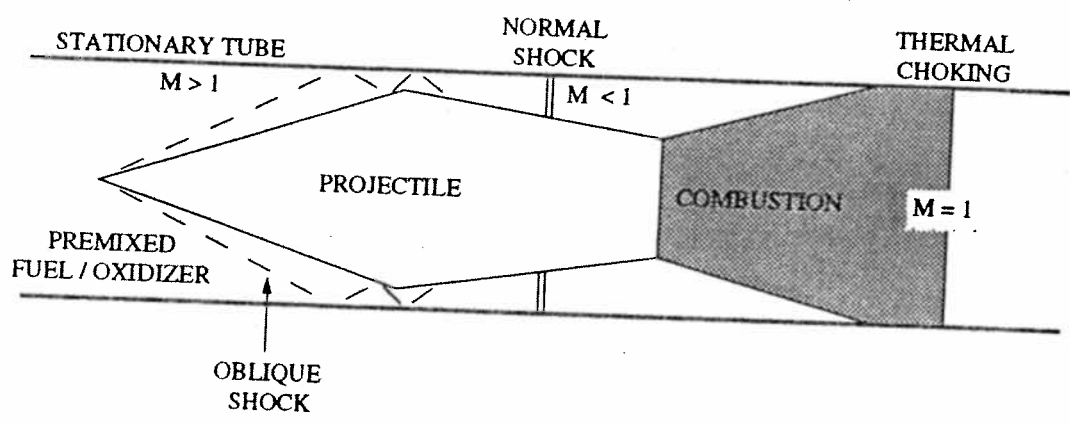
Fig. 2: Ram Accelerator.

II. EXPERIMENTAL APPARATUS

The ram accelerator experimental facility at the University of Washington was established in 1985. In 1990, this facility received a massive system upgrade, and a description of the improved facility appears below. The recent development of a densely instrumented tube section now provides high resolution data, as well. Typical ram accelerator projectile and obturator designs have also been firmly established through extensive experimentation.

EXPERIMENTAL FACILITY

The ram accelerator facility consists of three main components: the light gas gun, the ram accelerator section, and the decelerator section. A schematic of the experimental facility appears in Fig. 3. The light gas gun measures 6 m in length; it consists of a driver with a double aluminum diaphragm and a launch tube. The projectile is initially secured within the launch tube immediately downstream from the diaphragm. The driver is filled with helium at pressures up to 5000 psi, the diaphragm is burst, and the projectile/obturator combination accelerates through the launch tube. The launch tube has a 38 mm bore and is connected to a perforated wall tube enclosed within an evacuated dump tank. This perforated tube vents the helium driver gas prior to projectile entrance into the ram accelerator section. This single stage light gas gun launches projectile/obturator

combinations with total masses ranging between 70 g and 110 g to muzzle velocities up to 1300 m/sec.

The ram accelerator section measures 16 m in length and is composed of eight 2 m long steel tubes with a 38 mm bore and an outer diameter of 100 mm. A total of 40 instrumentation stations are located at 40 cm intervals along the tube. Each tube contains five instrumentation stations which alternate between three stations with four diametrically opposed ports situated radially at 90° angles to each other and two stations with three ports situated radially at 120° to each other, yielding a total of 144 instrument ports. These ports accommodate any combination of electromagnetic transducers [10], which detect projectile position, and piezoelectric pressure transducers, fiber optic probes [11], and thin film thermocouples [12] which each measure specific flow properties at the tube wall. Information from these transducers is collected through a 1-MHz 32-channel digital data acquisition system, which can monitor 100 separate data inputs through multiplexing.

Thin mylar diaphragms are used to seal both the entrance and exit of the ram accelerator section, as well as to separate gas mixtures in successive stages. Typical gas mixtures contain methane, oxygen, and various diluents such as nitrogen, helium, hydrogen, or excess methane. The addition of diluent gases adjusts the sound speed and energy density of the mixture. The flow rate of each gas is regulated independently by sonic orifices. The gases are then mixed and directed to the appropriate tube sections. The ram

accelerator tubes are designed to operate safely at a maximum fill pressure of 50 atm.

Finally, the end of the ram accelerator section is connected to a 0.76 m drift tube, which allows the projectile to exit into an evacuated, final dump tank. This tank has a length of 2.4 m and is equipped with two 25 cm diameter windows, located on either side of the tank at the midpoint, for photography purposes. The catcher tube, a 1 m long tube with a 20 cm bore, extends upstream from the terminal end of the dump tank. Either aluminum or steel witness plates, along with tightly packed rug remnants, are placed in the catcher tube to stop the projectile.

DENSELY INSTRUMENTED SECTION

The present ram accelerator tubes provide data useful in a global performance analysis. Transient activities, however, often have considerably shorter time scales, which cannot be accommodated by instruments placed at the standard 40 cm separation. Consequently, a densely instrumented ram accelerator section was developed to provide data with higher temporal resolution [13]. A schematic of this densely instrumented section appears in Fig. 4. It measures 21 cm in length. The tube couplers at either end allow the densely instrumented section to be mounted between any pair of existing tubes. Consequently, to observe the mixture transition process, the densely instrumented section was initially placed immediately downstream from the Mylar diaphragms separating the first and second stage mixtures.

A total of eight instrumentation stations are located at 20 mm intervals along the densely instrumented tube section. Each station contains four diametrically opposed instrument ports situated at 90° angles to each other, and successive stations are rotated by 45°, as indicated in Fig. 4. As the projectile travels through the densely instrumented section, data are collected simultaneously at eight stations along the projectile length, as opposed to the more spatially intermittent data collection in the original ram accelerator tubes.

PROJECTILE AND OBTURATOR DESIGN

The standard ram accelerator projectile configuration is shown in Fig. 5. The projectile is manufactured from 7075-T6 aluminum as two separate pieces: the nose cone and the body. These components are hollow to minimize projectile mass, thus reducing the required gas fill pressures within the ram accelerator tubes, as well as the light gas gun. The two pieces thread together at the throat. Typical projectile masses range between 60 g and 90 g.

The ram accelerator projectile incorporates a nose cone half-angle of 10° and a body length of 7.1 cm. Early projectiles included an octagonal body cross section for machining convenience. More recent projectiles, however, are fabricated with computer numerically controlled machines and utilize a smoothly rounded cross section. The body segment is machined with four integral fins to center the projectile within the tube. The fins have a nominal

thickness of 3.8 mm, and total clearance between the fins and the tube wall is 0.1 mm.

A thin magnetic annulus is placed at the junction between the nose cone and the projectile body, and a small magnetic disk can be situated at the base of the projectile. The electromagnetic transducers detect these magnets as the projectile passes by, providing a distance-time history of the experiment, and, thus, the projectile velocity.

The ram accelerator projectile is launched with the assistance of an obturator secured on the rear projectile face in the configuration shown in Fig. 6. Figure 7 displays the typical ram accelerator obturator design. The obturator is manufactured from Lexan polycarbonate as two components: the obturator piece and the back plate. The obturator piece has a diameter of 38 mm and contains 19 axial perforations at regular intervals. The back plate is simply a disk initially affixed to the obturator piece to provide a solid, flat surface for the driver gas in the light gas gun to push against. As the obturator impacts the gas mixture, it generates a normal shock, which ignites the combustible gas mixture and travels forward on to the projectile body. The back plate subsequently detaches from the obturator, exposing the axial holes to the flow. These holes mechanically choke the flow behind the projectile, stabilizing the normal shock position along the projectile body as combustion starts [14, 15].
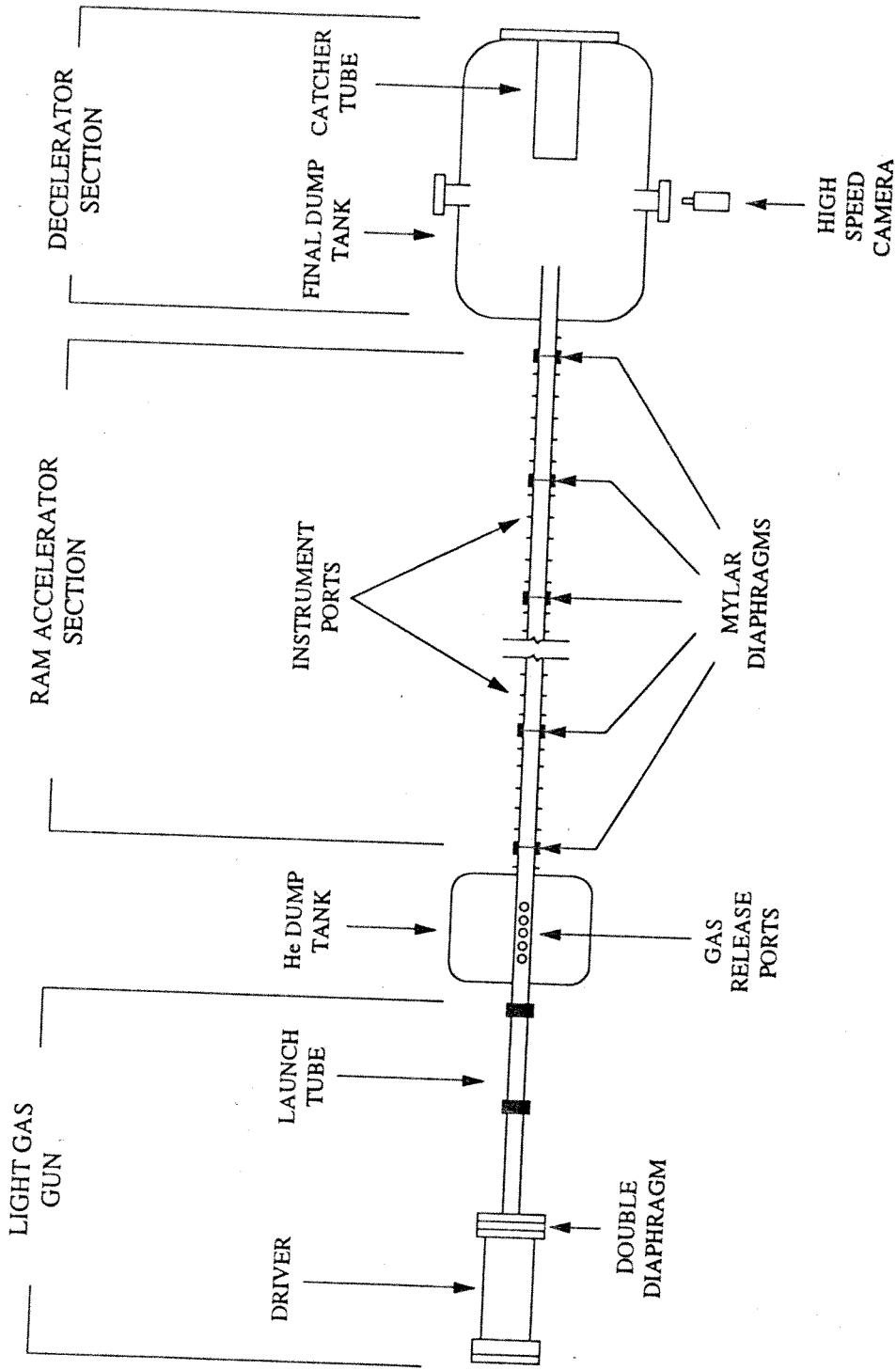
Fig. 3: Ram Accelerator Experimental Facility.
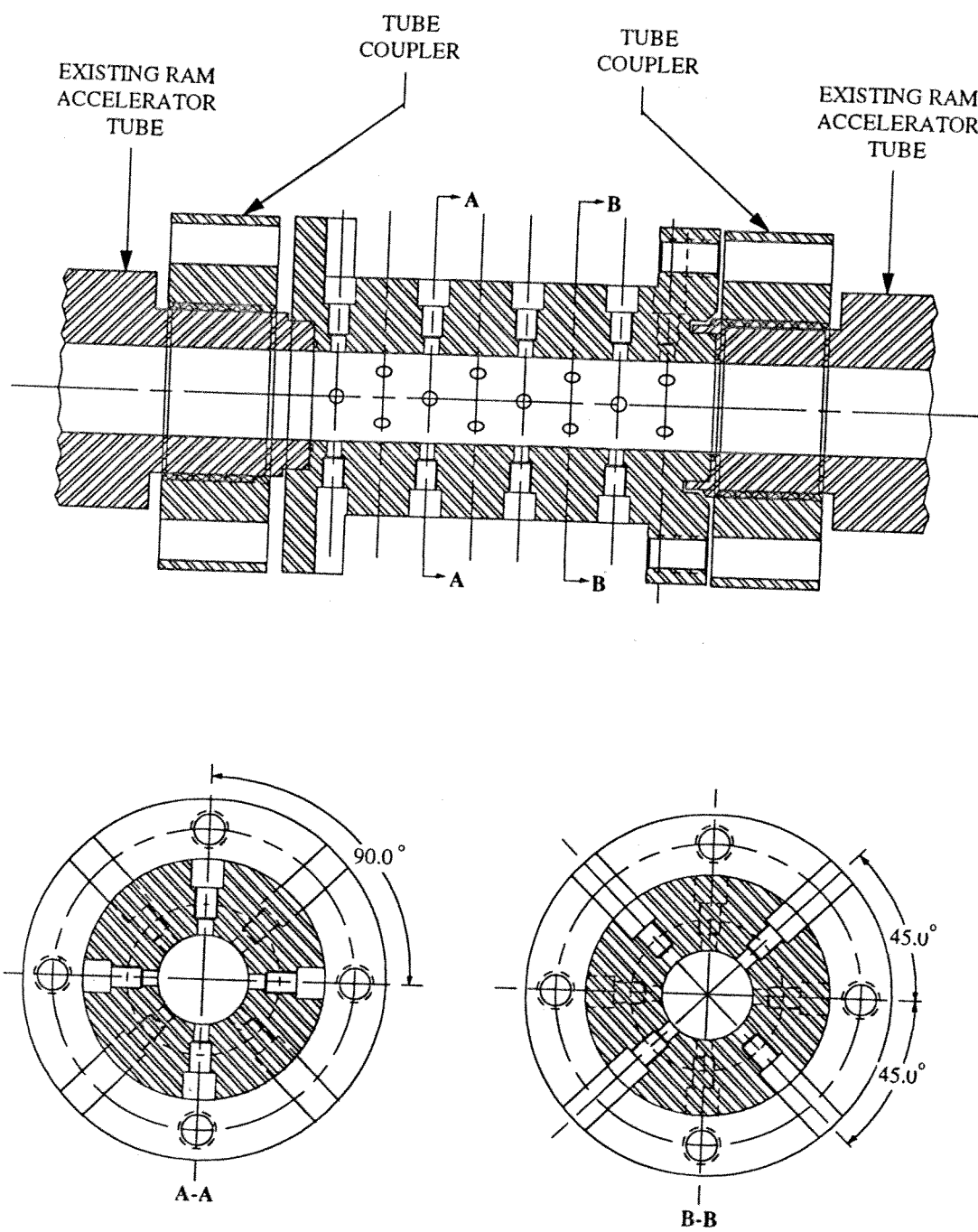
Fig. 4: Densely Instrumented Ram Accelerator Section.
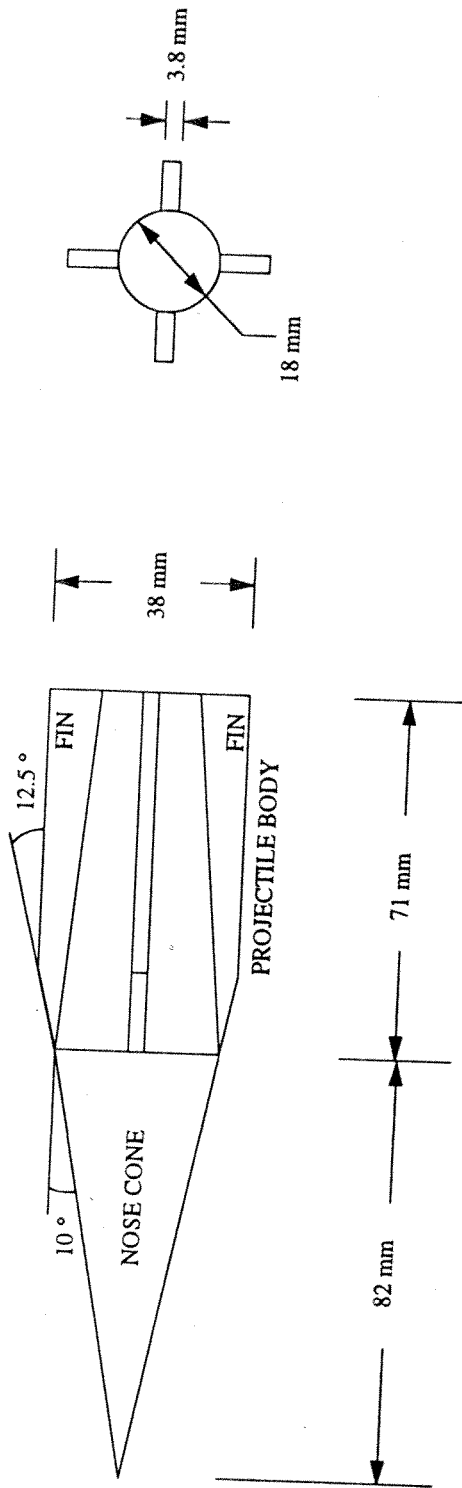
Fig. 5: Ram Accelerator Projectile.

PROJECTILE   OBTURATOR
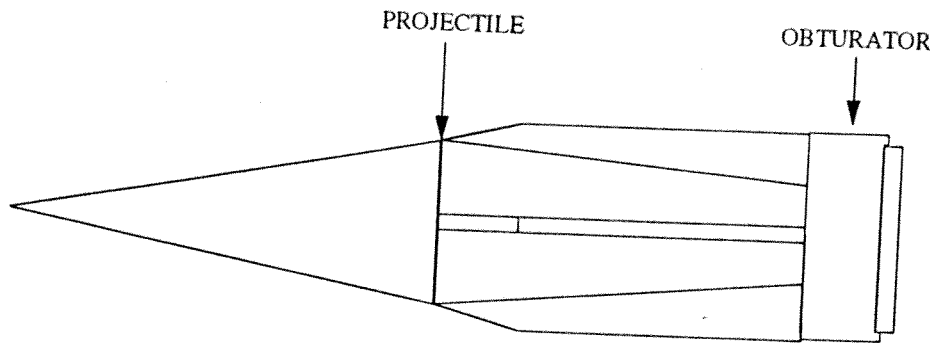
Fig. 6: Ram Accelerator Projectile at Launch.

5 mm DIA.
(19 HOLES)

16 mm   2.5 mm

38 mm

OBTURATOR
PIECE

OBTURATOR   BACK PLATE

FRONT VIEW

(BACK PLATE
REMOVED)

SECTION VIEW

(HOLES
REMOVED)
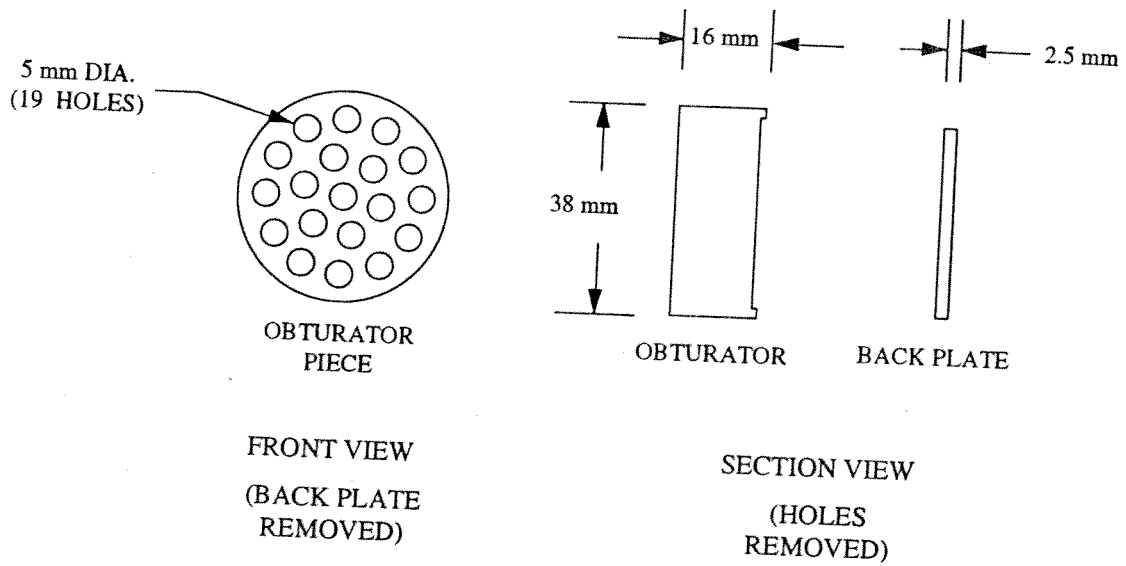
Fig. 7: Ram Accelerator Obturator.

III. RAM ACCELERATOR OPERATION

Three different modes of ram accelerator operation have been studied both experimentally and theoretically [3,8]. These operating regimes are defined by the projectile velocity and the C-J velocity of the gas mixture. The thermally choked propulsion mode is observed at subdetonative velocities, or velocities below approximately 85% of the C-J speed. The transdetonative propulsion mode encompasses projectile velocities between approximately 85% and 115% of the C-J detonation speed. Finally, at projectile velocities in excess of 115% the C-J velocity, a superdetonative propulsion mode occurs.

THERMALLY CHOKED PROPULSION MODE

The thermally choked ram accelerator propulsion mode has received considerable attention both experimentally and theoretically [3,16,17]. This propulsive mode is observed at projectile velocities up to approximately 85% the mixture C-J speed. Figure 8 displays a diagram of a projectile during thermally choked operation. The projectile entrance velocity and the gas mixture in the ram accelerator section are selected to provide an initial Mach number sufficient to aerodynamically "start" the diffuser. The nominal starting Mach number lies between 2.3 and 2.8 [16].

Upon entrance to the test section the projectile generates a conical bow shock which reflects successively between the ram accelerator tube and the projectile, itself. A normal shock located on the projectile body reduces the initially supersonic flow to subsonic flow, inducing a high pressure region on

the rear of the projectile and a low pressure region on the front. Consequently, forward thrust is produced, and the projectile accelerates through the tube. During thermally choked operation, neither the oblique shock system nor the normal shock initiate combustion. All chemical reactions occur within the zone of subsonic flow behind the projectile. The heat released by the exothermic reactions thermally chokes the flow behind the projectile, thus stabilizing the normal shock on the projectile body.

Representative electromagnetic, pressure, and luminosity data obtained from a single station during thermally choked operation appear in Fig. 9. The electromagnetic signals resulting from the magnets placed onboard the projectile determine a projectile reference position for pressure and fiber optic signal output. The initial rise in the pressure signal indicates the initial conical shock, and the first and second peaks correspond, respectively, to its reflections from the projectile impinging on the tube wall. A sharp pressure rise denotes the normal shock. The pressure increases abruptly behind this normal shock, and then it diminishes as a result of the subsonic heat addition to choking and the subsequent non-steady expansion of the combustion products.

Data from the fiber optic transducer indicate significant light emission from the combustion zone behind the projectile. Light emission is associated with the presence of combustion. Since most gas mixtures utilize methane/oxygen combustion reactions in fuel-rich ratios, carbon particles, or soot, form as combustion products and emit blackbody radiation. Therefore,

the peak light intensity is thought to correspond with the peak blackbody emission, and thus the maximum gas temperature.

Various computational models for the thermally choked ram accelerator propulsion mode have been developed [14,18,19]. Pressure histories determined by axisymmetric and pseudo-one dimensional models exhibit the same qualitative trends as data gathered experimentally. Another model applies conservation equations to a control volume surrounding the projectile [16]. All model predict that the normal shock travels toward the rear of the projectile as projectile velocity increases. Ultimately, the normal shock falls off the base of the projectile, reducing the thrust to zero. In the extreme case of a projectile tapering to a point at the base, the normal shock moves off the projectile at full tube area in front of the combustion zone. A normal shock wave in a constant area duct followed by a finite reaction zone resulting in thermally choked, steady flow is defined as a C-J detonation wave. Therefore, the maximum velocity predicted for thermally choked ram accelerator operation is the C-J detonation speed of the gas mixture.

TRANSDETONATIVE PROPULSION MODE

The transdetonative propulsive mode of the ram accelerator is defined at projectile velocities between approximately 85% and 115% of the C-J speed of the gas mixture. The projectile acceleration within this velocity range often greatly exceeds the expectations of thermally choked operation [20,21]. A simplified physical model of the transdetonative mode has not yet been

developed. Experimental data, however, suggests that combustion along the projectile body may play a critical role.

Figure 10 illustrates nominal electromagnetic, pressure and fiber optic data obtained during transdetonative ram accelerator operation. Again, the magnetic signals define the position of the projectile relative to the pressure and luminosity profiles. The pressure peaks generated by the conical shock and its reflections are stronger and steeper than those observed during thermally choked operation, and is consistent with the increased projectile Mach number. Also, the distinct normal shock evident during thermally choked operation is replaced by a more gradual pressure rise, probably due to combustion along the projectile, itself.

The output from the fiber optic light sensor reveals substantial light emission along both the projectile body and nose cone, possibly the result of shock-induced or boundary layer combustion. As the projectile continues to accelerate, the light output along the projectile increases. The subsonic combustion zone, however, behind the projectile remains the dominant region for chemical reactions, as illustrated by the significant light output following the projectile. Since heat addition along the body occurs at supersonic velocities, the transdetonative propulsion mode exhibits both supersonic and subsonic heat addition.

Currently, transdetonative propulsion is not fully understood and remains the topic of considerable research, particularly investigations into the location, magnitude, and source of combustion along the projectile. Consequently, transdetonative operation has not been modeled as extensively

as the thermally choked operating mode. A pseudo-one dimensional model incorporating heat addition along the projectile body, however, has been developed which successfully reproduces experimental projectile velocity profiles [19].

SUPERDETONATIVE PROPULSION MODE

Transdetonative propulsion often allows projectiles to successfully make a transition from subdetonative velocities to velocities in excess of 115% the C-J speed of the gas mixture. At projectile velocities above 115% of the C-J speed, a superdetonative propulsion mode occurs [22]. The physical characteristics of superdetonative propulsion remain speculative. A schematic of one proposed model utilizing oblique detonation waves, however, appears in Fig. 11. The gas dynamic principles of this oblique detonation mode resemble those of the Oblique Detonation Wave Engine [23].

As during thermally choked operation, the initial conical shock does not ignite the flow. In the oblique detonation mode, however, the first reflected shock from the tube wall does initiate combustion, creating an oblique detonation wave. The pressure rises in the region immediately behind the oblique detonation wave as heat is added supersonically, thus accelerating the projectile.

Data obtained during superdetonative operation appear in Fig. 12. The initial conical shock is steeper and stronger in magnitude than during either thermally choked or transdetonative operation as a consequence of the increased projectile Mach number. Also, as observed during transdetonative

operation, the normal shock is replaced by a more gradual pressure rise, most likely the result of combustion along the projectile.

The luminosity data indicate significant light emission along the entire projectile and a lesser amount from the combustion zone. Therefore, the supersonic heat addition along the projectile, possibly due to shock-induced combustion, appears more dominant than the subsonic combustion behind the projectile.

A numerical model of the superdetonative propulsion mode described above has been developed [24]. This model uses an 8 reaction combustion model involving 7 different chemical species to predict ram accelerator performance at velocities between 5 km/sec and 10 km/sec. These results suggest the presence of an oblique detonation wave along the projectile and reveal anticipated pressure and temperature profiles at these high velocities.
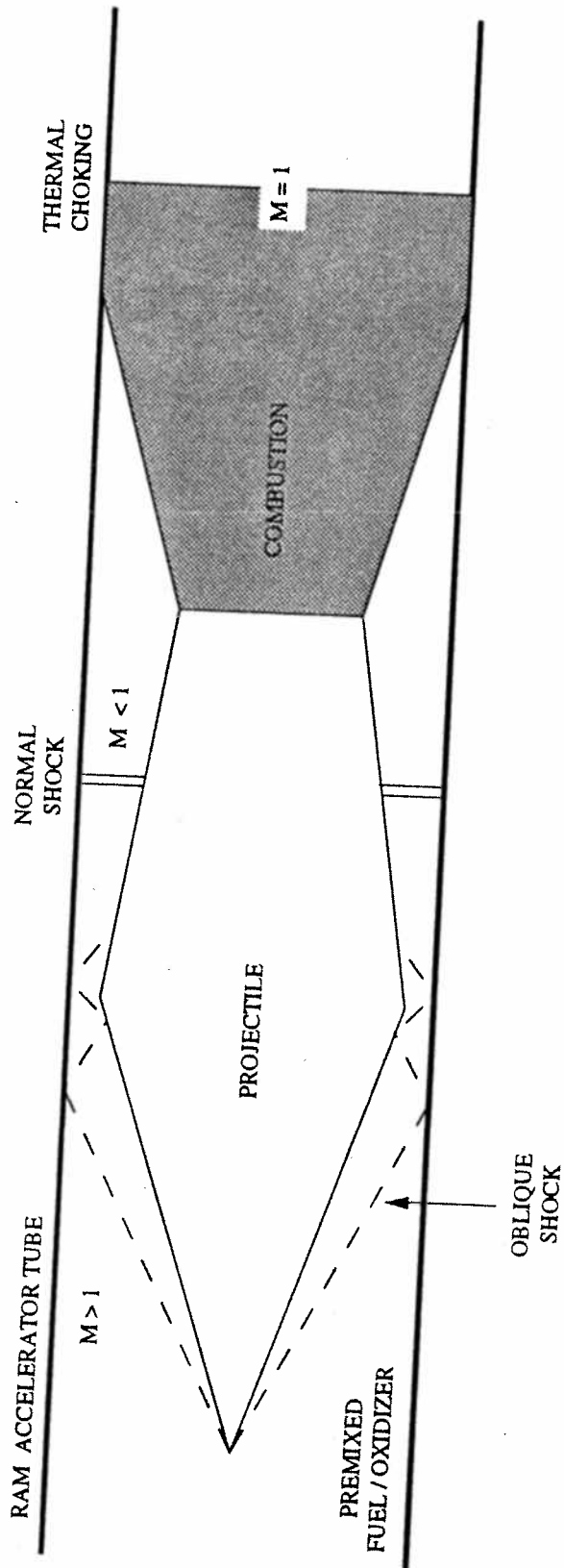
Fig. 8: Thermally Choked Propulsion Mode.
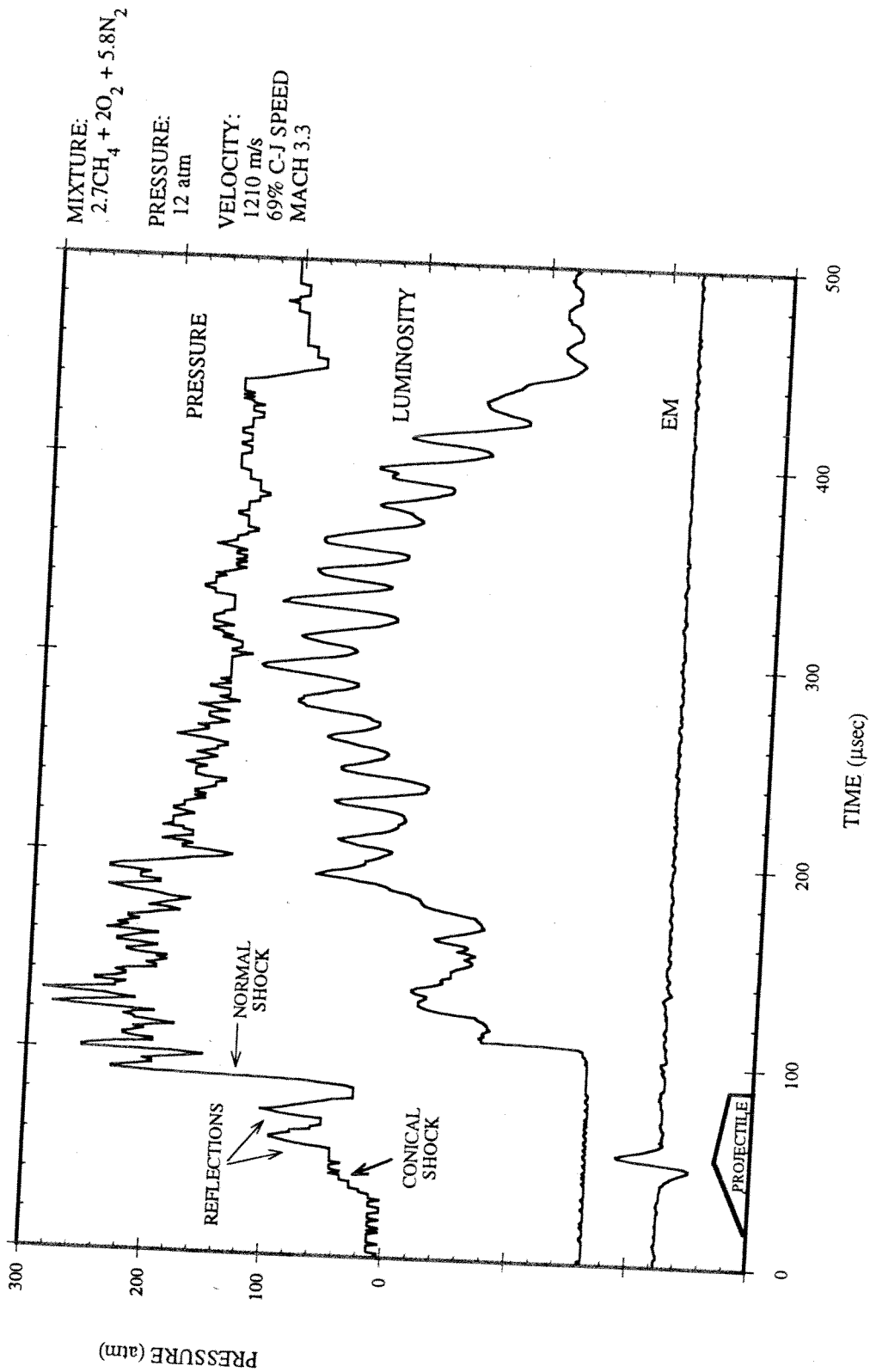
Fig. 9: Representative Data from Thermally Choked Propulsion Mode.
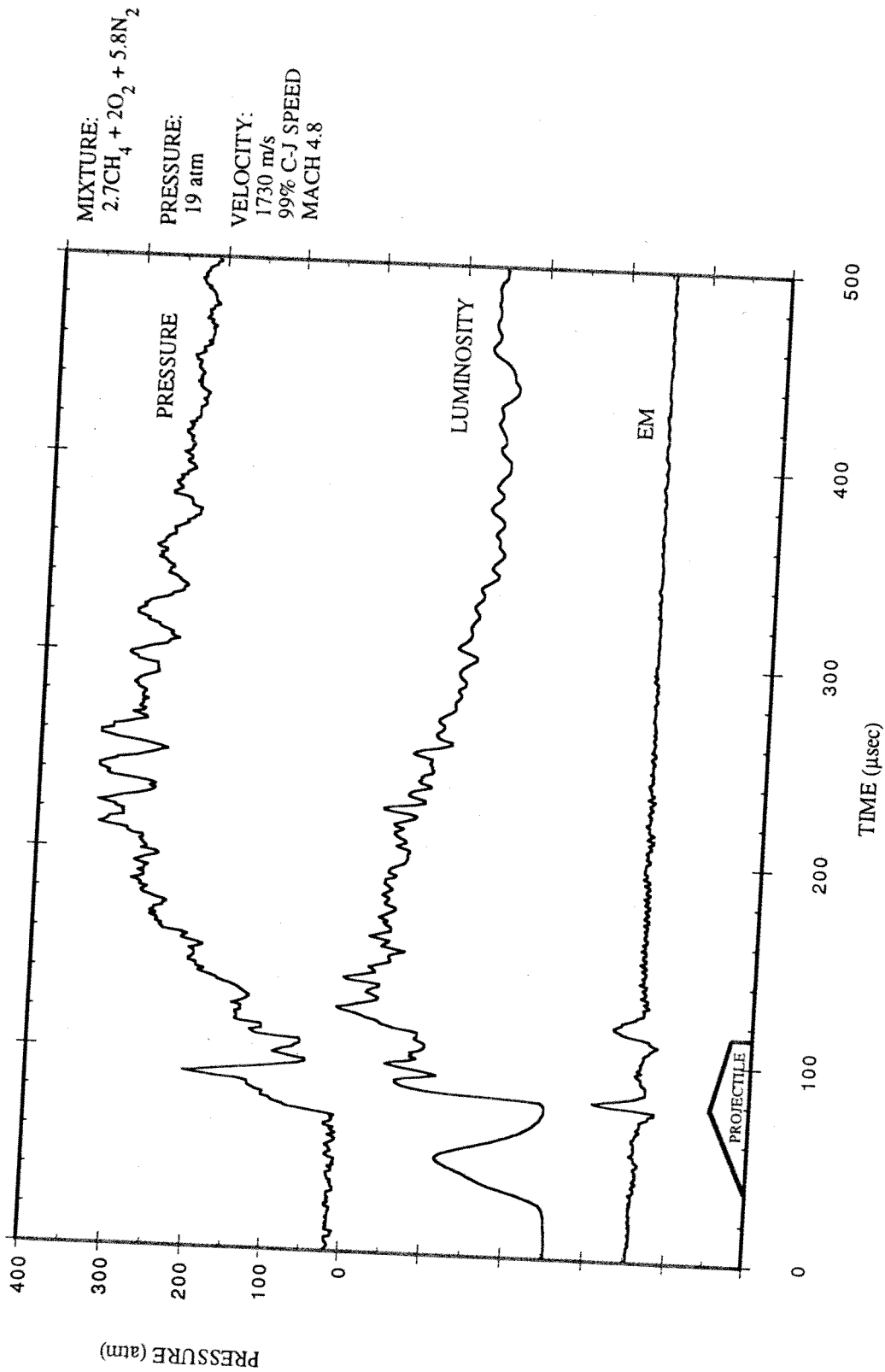
Fig. 10: Representative Data from Transdetonative Propulsion Mode.
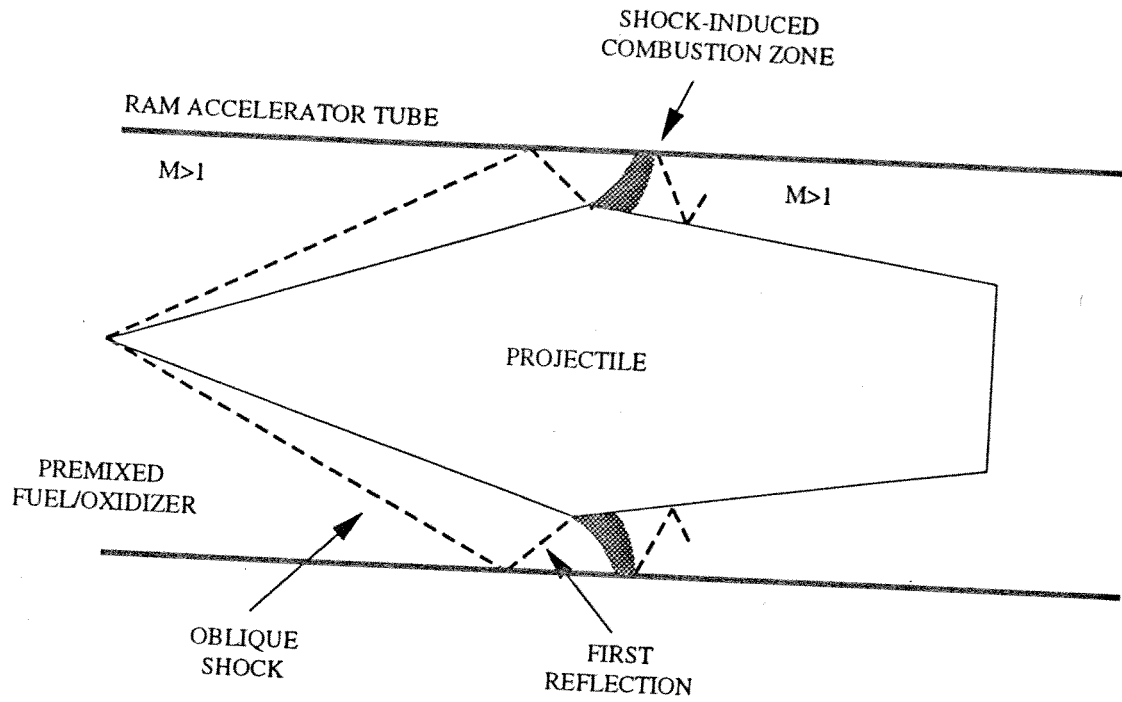
Fig. 11: Oblique Detonation Mode.
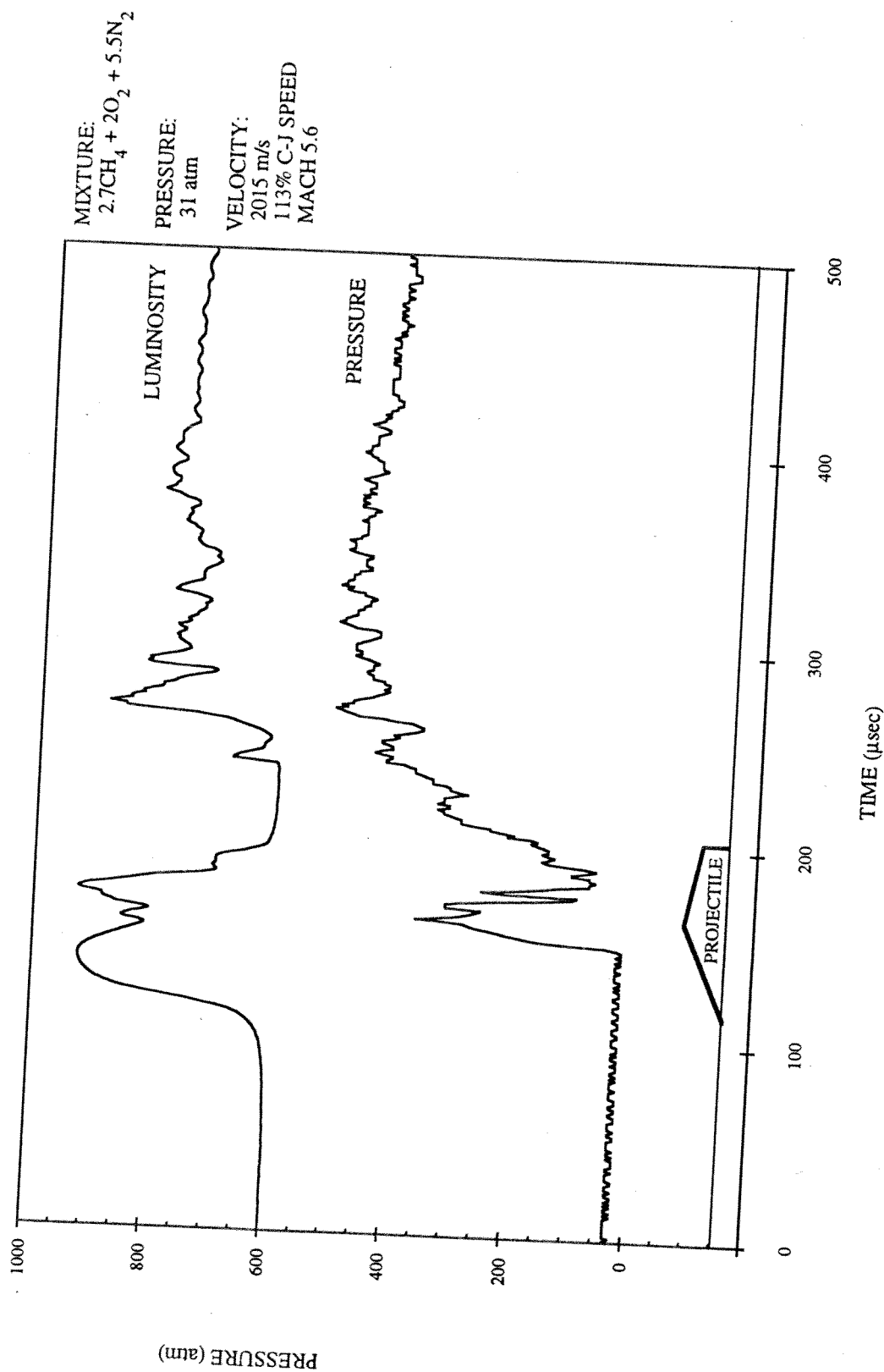
Fig. 12: Representative Data from Superdetonative Propulsion Mode.

IV. MATHEMATICAL PRINCIPLES

The numerical method selected to model the oblique shock system during the ram accelerator transition process utilizes the two dimensional Euler equations. These equations are rewritten as vector equations in conservation law form to enhance shock capturing abilities. Finally, the Euler equations are transformed from Cartesian coordinates to generalized coordinates for application to arbitrary geometries.

EULER EQUATIONS

The Euler equations govern fluid motion through the conservation of mass, momentum, and energy. The Euler equations in scalar form appear below.

Conservation of mass:

$$\frac{\partial \rho}{\partial t} + \frac{\partial}{\partial x_i}(\rho u_j) = 0$$

Conservation of momentum:

$$\frac{\partial}{\partial t}(\rho u_i) + \frac{\partial}{\partial x_j}(\rho u_i u_j) = -\frac{\partial p}{\partial x_i}$$

Conservation of energy:

$$\frac{\partial}{\partial t}\left(\rho \epsilon + \frac{1}{2}\rho u_i u_i\right) + \frac{\partial}{\partial x_j}\left[\left(\rho \epsilon + \frac{1}{2}\rho u_i u_i\right)u_j\right] = -\frac{\partial}{\partial x_i}(p u_i)$$

where ρ represents the fluid density, t indicates time, x_i and u_i indicate the position and velocity components in the ith direction, respectively, ε represents the internal energy per unit mass, and p represents the fluid pressure.

It should be noted that the Euler equations deviate from the full Navier-Stokes equations through the omission of viscosity and thermal conductivity terms. In this ram accelerator model, however, the effects of both viscosity and thermal conductivity are deemed secondary in importance to convective terms. Consequently, the Euler equations provide an appropriate equation set.

CONSERVATIVE FORM OF THE EULER EQUATIONS

The Euler equations must be rewritten in conservative form to effectively capture discontinuities. The conservative form of the two dimensional Euler equations in Cartesian coordinates is shown below.

$$\frac{\partial Q}{\partial t} + \frac{\partial F}{\partial x} + \frac{\partial G}{\partial y} = S - H$$

where

$$Q = \begin{bmatrix} \rho \\ \rho u \\ \rho v \\ e \end{bmatrix}$$

$$F=\begin{bmatrix} \rho u \\ \rho u^2 + p \\ \rho uv \\ u(e+p) \end{bmatrix} \quad ; \quad G=\begin{bmatrix} \rho v \\ \rho uv \\ \rho v^2 + p \\ v(e+p) \end{bmatrix}$$

$$S=\begin{bmatrix} 0 \\ 0 \\ 0 \\ \Delta q \end{bmatrix} \quad ; \quad H=\frac{1}{r}\begin{bmatrix} \rho v \\ \rho uv \\ \rho v^2 \\ v(e+p) \end{bmatrix}$$

The vector Q contains the conservation variables, mass, momentum in the horizontal (x) and vertical (y) directions, and energy, all defined on a unit volume basis. The velocity in the horizontal direction is denoted by u, while the velocity in the vertical direction is indicated by v. The energy per unit volume, e, is defined as:

$$e=\rho\epsilon+\frac{1}{2}\rho\left(u^2+v^2\right)$$

The vectors F and G contain flux terms in the horizontal and vertical directions, respectively. The right hand side of the vectorized Euler equations contains both a traditional source term S, which contains an optional heat addition term Δq, and an axisymmetric term H, with radial dimension r.

The conservative Euler equations are solved in conjunction with the equation of state for a perfect gas, as shown below.

$$p=(\gamma-1)(e-\frac{1}{2}\rho(u^2+v^2))$$

where γ represents the ratio of specific heats.

As a final simplification, all variables are normalized to avoid dimensional quantities. The dimensionless variables in terms of characteristic reference quantities are defined below.

$$\rho^* = \frac{\rho}{\rho_\infty}$$

$$u^* = \frac{u}{c_\infty}$$

$$v^* = \frac{v}{c_\infty}$$

$$p^* = \frac{p}{\rho_\infty c_\infty^2}$$

$$e^* = \frac{e}{\rho_\infty c_\infty^2}$$

$$t^* = \frac{t c_\infty}{L}$$

$$x^* = \frac{x}{L}$$

$$y^* = \frac{y}{L}$$

The subscript ∞ denotes a predesignated freestream value, c represents the acoustic speed of the gas mixture, and L indicates a characteristic length, defined as the ram accelerator tube diameter. The superscript $*$, which indicates the dimensionless form of the variable, is omitted from the following discussions. The conservative form of the Euler equations remains unchanged with the substitution of nondimensional variables.

GENERALIZED COORDINATES

The Euler equations in the form presented above utilize a Cartesian coordinate system. Different geometries, however, are more suited to alternate coordinate systems. Therefore, the Euler equations must be modified to solve problems with arbitrary geometries. Figure 13 illustrates a one-to-one mapping of points in the physical plane, defined by the coordinates x and y and time parameter t, to points in the computational plane, defined by ξ and η and time parameter τ. In general, an unsteady grid may be defined by a set of transformations, as shown below.

$$\xi = \xi(x,y,t)$$
$$\eta = \eta(x,y,t)$$
$$t = \tau$$

The partial derivatives in the Euler equations are redefined with the chain rule of differentiation, as illustrated with the time derivative, below.

$$\frac{\partial Q}{\partial t} = \frac{\partial Q}{\partial \tau} + \frac{\partial Q}{\partial \xi}\frac{\partial \xi}{\partial t} + \frac{\partial Q}{\partial \eta}\frac{\partial \eta}{\partial t}$$

By expanding the other partial derivatives in a similar manner, the coordinate transformation below is defined.

$$\begin{bmatrix} \partial_t \\ \partial_x \\ \partial_y \end{bmatrix} = \begin{bmatrix} 1 & \xi_t & \eta_t \\ 0 & \xi_x & \eta_x \\ 0 & \xi_y & \eta_y \end{bmatrix} \begin{bmatrix} \partial_\tau \\ \partial_\xi \\ \partial_\eta \end{bmatrix}$$

where a subscripted variable indicates partial differentiation with respect to that variable. The same procedure with the inverse grid transformation yields a similar expression defining the inverse transformation.

$$\begin{bmatrix} \partial_\tau \\ \partial_\xi \\ \partial_\eta \end{bmatrix} = \begin{bmatrix} 1 & x_\tau & y_\tau \\ 0 & x_\xi & y_\xi \\ 0 & x_\eta & y_\eta \end{bmatrix} \begin{bmatrix} \partial_t \\ \partial_x \\ \partial_y \end{bmatrix}$$

Since these transformations are inverses of each other, the following terms may be derived.

$$\xi_x = J y_\eta$$
$$\xi_y = -J x_\eta$$
$$\xi_t = J(-x_\tau y_\eta + y_\tau x_\eta)$$
$$\eta_x = -J y_\xi$$
$$\eta_y = J x_\xi$$
$$\eta_t = J(x_\tau y_\xi + y_\tau x_\xi)$$

The quantities x_ξ, x_η, y_ξ, and y_η are calculated with second order finite differencing techniques assuming $\Delta x = \Delta h = 1$. The terms ξ_x, η_x, ξ_y, and η_y are defined as the gridmetrics, and the variable J refers to the Jacobian, as defined below.

$$J^{-1} = x_\xi y_\eta - x_\eta y_\xi$$

The gridmetrics and the Jacobian are used to write the Euler equations for generalized coordinates. First, the Euler equations must be expanded via the chain rule, as illustrated previously. The expanded form appears below.

$$\frac{\partial Q}{\partial \tau} + \xi_t \frac{\partial Q}{\partial \xi} + \eta_t \frac{\partial Q}{\partial \eta} + \xi_x \frac{\partial F}{\partial \xi} + \eta_x \frac{\partial F}{\partial \eta} + \xi_y \frac{\partial G}{\partial \xi} + \eta_y \frac{\partial G}{\partial \eta} = S - H$$

Unfortunately, however, this equation is not conservative. The conservative form is achieved, however, by multiplying by J^{-1} and combining terms through differentiation by parts, as illustrated below.

$$J^{-1} \xi_x \frac{\partial F}{\partial \xi} = \frac{\partial}{\partial \xi} (J^{-1} \xi_x F) - F \frac{\partial}{\partial \xi} (J^{-1} \xi_x)$$

The Euler equations in generalized coordinates become:

$$\frac{\partial \tilde{Q}}{\partial t} + \frac{\partial \tilde{F}}{\partial \xi} + \frac{\partial \tilde{G}}{\partial \eta} = \tilde{S} - \tilde{H}$$

where the ~ indicates the modified vectors shown below,

$$\tilde{Q} = J^{-1} \begin{bmatrix} \rho \\ \rho u \\ \rho v \\ e \end{bmatrix}$$

$$\tilde{F} = J^{-1} \begin{bmatrix} \rho U \\ \rho u U + \xi_x p \\ \rho v U + \xi_y p \\ U(e+p) \end{bmatrix} \quad ; \quad \tilde{G} = J^{-1} \begin{bmatrix} \rho V \\ \rho u V + \eta_x p \\ \rho v V + \eta_y p \\ V(e+p) \end{bmatrix}$$

$$\tilde{S} = \begin{bmatrix} 0 \\ 0 \\ 0 \\ \Delta q \end{bmatrix} \quad ; \quad \tilde{H} = \frac{J^{-1}}{r} \begin{bmatrix} \rho v \\ \rho u v \\ \rho v^2 \\ v(e+p) \end{bmatrix}$$

and U and V represent the contravariant velocities defined as:

$$U = \xi_t + \xi_x u + \xi_y v$$
$$V = \eta_t + \eta_x u + \eta_y v$$

The contravariant velocities are scaled velocities parallel to the grid lines. It should be noted, however, that these velocities are not necessarily perpendicular to each other.
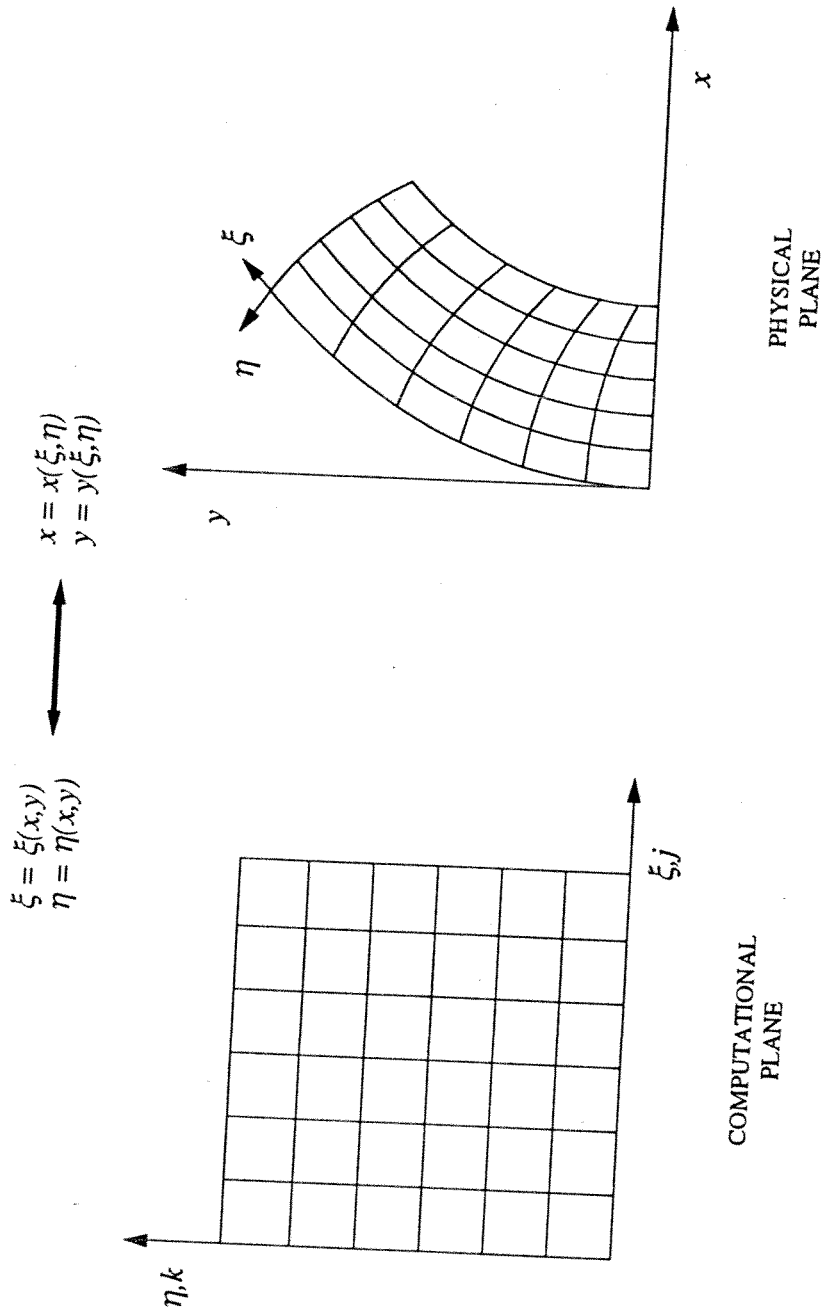
Fig. 13: Transformation from Physical Plane to Computational Plane.

V. COMPUTATIONAL MODEL

A numerical model of ram accelerator operation and mixture transition has been developed. This model emphasizes the oblique shock structure and its behavior during mixture transition. Therefore, it should be noted that the normal shock is not simulated, and a heat addition model is unnecessary. The computational domain surrounds an axisymmetric projectile. A MacCormack predictor/corrector method solves the governing Euler equations with the appropriate initial conditions and boundary conditions. Tests against established experimental results validated the numerics prior to implementation on actual ram accelerator transition cases.

COMPUTATIONAL DOMAIN

Figure 14 displays the computational domain selected for this numerical simulation. The domain surrounds a projectile profile and measures 80 x 20 grid points.

The projectile modeled in this study has a 10° nose cone half-angle, a 71 mm body length, and 14.5 mm throat radius. The base radius of 9.1 mm is determined from an effective base blockage area, which includes the blockage area of the fins on the physical projectile. The rear surface of the projectile incorporates a 10° tapered face to more easily capture any expansion about the projectile base. Finally, the vertical height of the domain equals the tube radius of 19 mm.

MacCORMACK METHOD

The MacCormack method is selected to solve the governing Euler equations [25,26]. This numerical algorithm uses a two step predictor/corrector approach, as defined below.

Predictor:

$$\overline{Q}_{j,k}^{n+1} = \tilde{Q}_{j,k}^{n} - dt\left(\tilde{F}_{j,k}^{n} - \tilde{F}_{j-1,k}^{n}\right) - dt\left(\tilde{G}_{j,k}^{n} - \tilde{G}_{j,k-1}^{n}\right) - dt\tilde{H}_{j,k}^{n} + dt\tilde{S}_{j,k}^{n}$$

Corrector:

$$\tilde{Q}_{j,k}^{n+1} = \frac{1}{2}\left[\tilde{Q}_{j,k}^{n} + \overline{Q}_{j,k}^{n+1} - dt\left(\overline{F}_{j+1,k}^{n+1} - \overline{F}_{j,k}^{n+1}\right) - dt\left(\overline{G}_{j,k+1}^{n+1} - \overline{G}_{j,k}^{n+1}\right) - dt\overline{H}_{j,k}^{n+1} + dt\overline{S}_{j,k}^{n+1}\right]$$

where j and k refer to position indices in the computational domain, n refers to the iteration number, and dt denotes the time increment. The overbar, $-$, indicates predicted values. The MacCormack algorithm uses the predictor to estimate values at the next time step, and the corrector combines the estimated values with the current values to determine the solution at the next time step. This MacCormack algorithm is second order in both space and time. It is explicit, time-accurate, and stable for Courant numbers less than unity.

In order to alleviate the oscillations inherent to the MacCormack method, a constant coefficient artificial dissipation scheme is employed [27,28]. The dissipation terms in both the ξ-direction and the η-direction, d_ξ and d_η, respectively, are defined , below.

$$d_\xi = -\epsilon_d \left(\tilde{Q}^n_{j-1,k} - 2\tilde{Q}^n_{j,k} + \tilde{Q}^n_{j+1,k} \right)$$
$$d_\eta = -\epsilon_d \left(\tilde{Q}^n_{j,k-1} - 2\tilde{Q}^n_{j,k} + \tilde{Q}^n_{j,k+1} \right)$$

The ϵ_d is the constant coefficient which dictates the magnitude of the dissipation. This constant is selected to adequately reduce oscillations while maintaining resolution and shock capturing capability.

INITIAL CONDITIONS

This ram accelerator transition model includes two computational steps and, consequently, two different initial conditions. First, all grid points are initialized with predesignated freestream conditions to obtain a supersonic profile. After the steady-state supersonic profile is achieved, it becomes the initial condition for transition calculations.

BOUNDARY CONDITIONS

The forward boundary of the computational domain consists of a supersonic inflow. Therefore, all flow variables are predetermined and remain constant throughout the computation. During transition calculations from one gas mixture to another, the properties of the second gas mixture enter at this forward boundary.

Both the upper and lower boundaries are modeled as inviscid, solid walls. The velocity normal to the wall, V_n, is fixed at zero, while the velocity tangent to the wall, V_t, is obtained through extrapolation from interior grid

points. The flow velocity components at the wall are then defined by the expression below.

$$\begin{bmatrix} u \\ v \end{bmatrix}_{wall} = \frac{1}{\sqrt{\eta_x^2 + \eta_y^2}} \begin{bmatrix} \eta_y & \eta_x \\ -\eta_x & \eta_y \end{bmatrix} \begin{bmatrix} V_t \\ V_n \end{bmatrix}$$

It should be noted that in generalized coordinates, the wall consists of a constant η line.

The pressure at the wall is obtained from the normal momentum equation in generalized coordinates, as defined below.

$$\left(\eta_x \xi_x + \xi_y \eta_y \right) p_\xi + \left(\eta_x^2 + \eta_y^2 \right) p_\eta = -\rho U \left(\eta_x u_\xi + \eta_y v_\xi \right)$$

The ξ derivatives are determined through central differencing, while the η derivatives incorporate first order, one-sided differencing. The solid wall is also assumed adiabatic, implying conservation of total enthalpy.

Finally, the rear boundary consists of a supersonic outflow. In supersonic flow, direct extrapolation from interior grid points yields the rear boundary values.

CODE VALIDATION

Prior to implementation on ram accelerator transition cases, the numerical model was validated against established experimental data. Since this model does not incorporate heat addition effects, the normal shock along the projectile body is not simulated. Therefore, the model was verified

against an experiment with a projectile travelling supersonically through the tube in the absence of combustion.

Figure 15 displays the pressure contours determined numerically for a projectile in supersonic flow. The oblique shock and its reflections are captured crisply with minimal dissipation. Figure 16 reveals the streamlines determined computationally. The streamlines illustrate the anticipated fluid flow pattern as each shock is encountered.

The numerical supersonic pressure profile at the tube wall appears in Fig. 17, while the corresponding experimental supersonic pressure profile is shown in Fig. 18. The initial conical shock denoted by the first pressure rise reaches a calculated value of approximately 50 atm, which compares well with the experimentally determined value of approximately 60 atm. The first reflection from the tube wall, indicated by the first sharp pressure peak, however, only reaches a calculated value of approximately 100 atm, nearly half the corresponding experimental measurement of 215 atm. It should be noted, though, that the initial conical shock is generated by the axisymmetric projectile nose cone. The first reflection, on the other hand, occurs along the projectile body and must encounter the projectile fins, resulting in three dimensional effects. Consequently, since the computational model is based on an axisymmetric projectile, it predicts the axisymmetric conical shock better than the refections. The qualitative tendencies of the reflections, however, are properly represented. Also, recent studies with the densely instrumented ram accelerator section have indicated that projectile orientation and inclination within the tube may result in unpredictable

pressure measurements [13]. Therefore, only qualitative comparisons between numerical and experimental results are made in the following discussions.

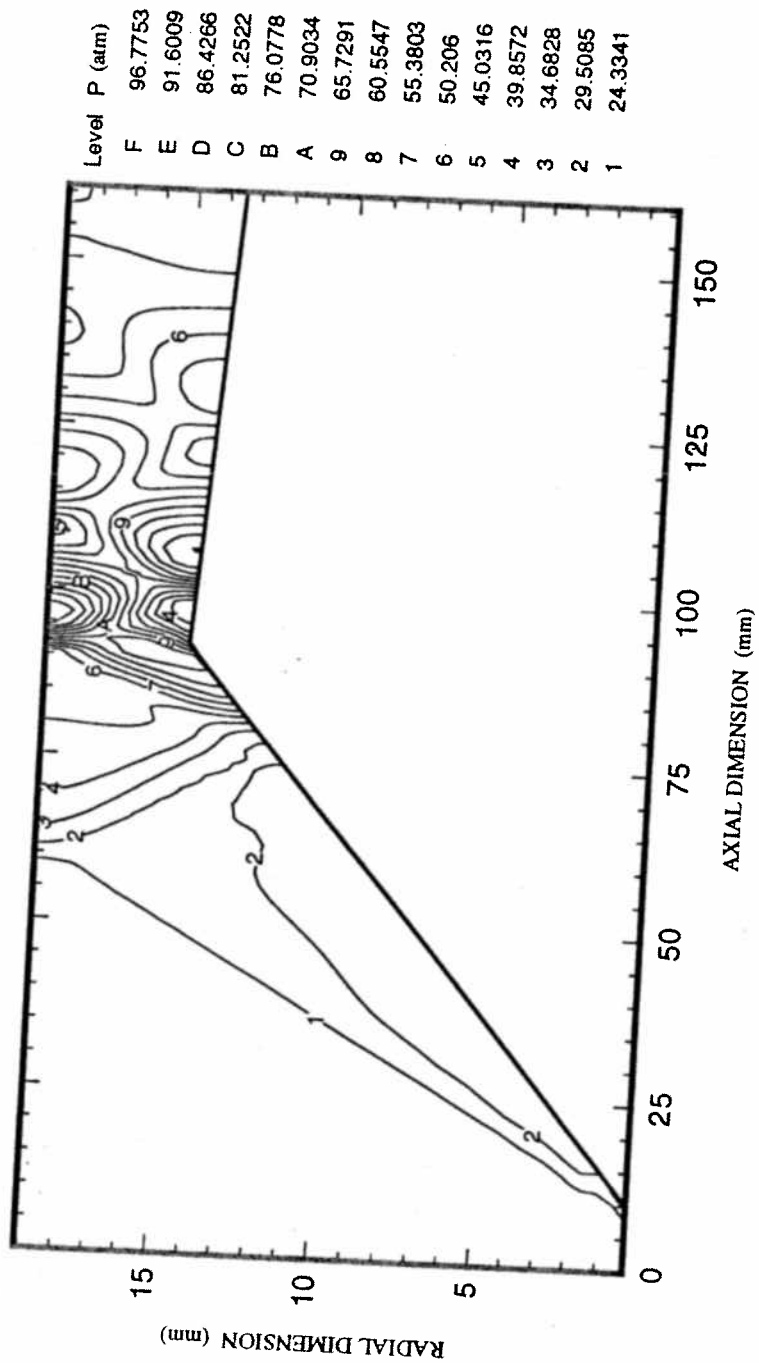| Level	P (atm)
F	96.7753
E	91.6009
D	86.4266
C	81.2522
B	76.0778
A	70.9034
9	65.7291
8	60.5547
7	55.3803
6	50.206
5	45.0316
4	39.8572
3	34.6828
2	29.5085
1	24.3341

Fig. 15: Pressure Contours Determined Numerically for Supersonic Flow.
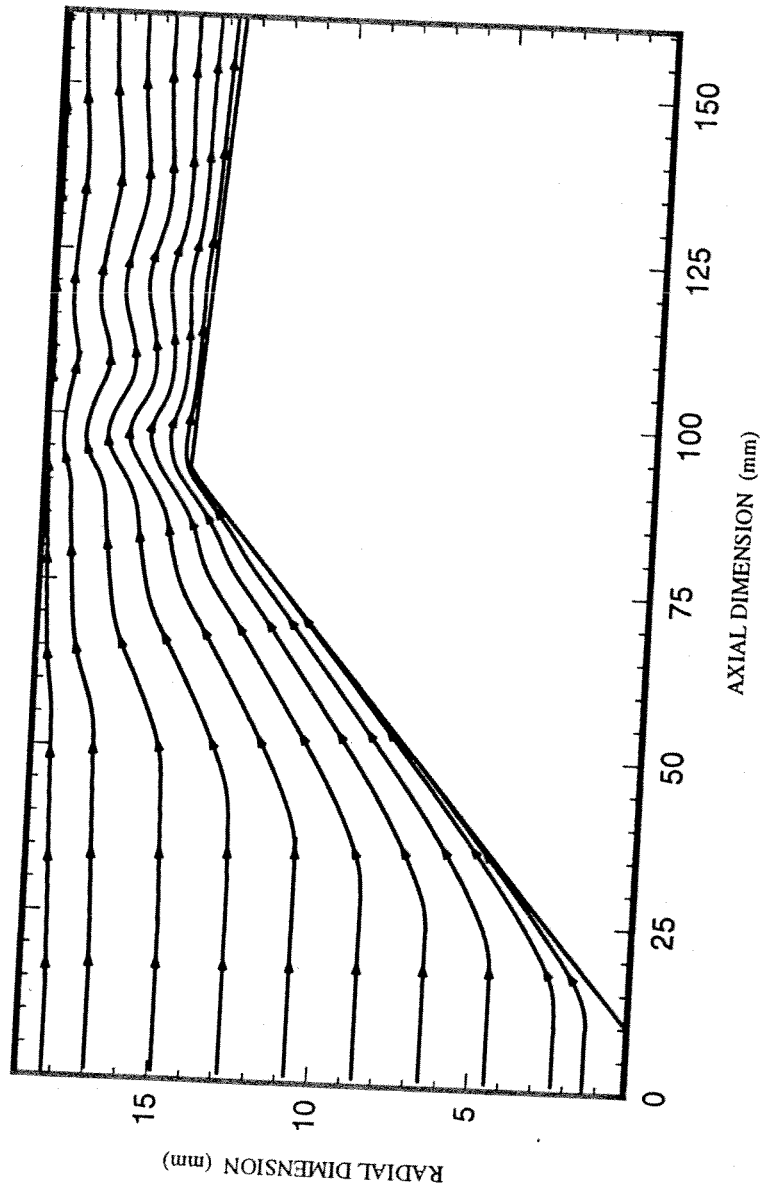
Fig. 16: Streamlines Determined Numerically
for Supersonic Flow.

transition in case 2 does not occur at a constant Mach number. The transition in case 2, however, occurs at a constant pressure.

In each experiment, the densely instrumented section was located at the beginning of the second gas mixture. The input parameters of the computational model have been selected to simulate the data obtained from the densely instrumented ram accelerator section for a comparison between numerical and experimental results.

CASE 1: CONSTANT MACH NUMBER TRANSITION

As indicated in Table 1, the projectile in the first experiment makes a transition from a mixture at a higher pressure to the same mixture at a lower pressure. Since the tube volume remains fixed, the density of the second stage mixture is reduced. The sound speed, however, remains constant between stages. Consequently, since the projectile velocity does not change appreciably in the time required to complete the transition, the Mach number during the mixture transition remains constant.

Figure 19 reveals the pressure contours and wall pressure profile determined computationally for a point prior to the transition. The pressure contours reveal a well established oblique shock system along the projectile. The initial conical shock appears in the wall pressure profile as the first pressure rise, and the first reflection from the projectile body appears as the sharp pressure peak.

Figure 20 depicts the first contact between the projectile and the second stage mixture. The pressure contours indicate that the conical shock

system remains unchanged, except in the forward region where a pressure wave has propagated on to the projectile nose cone. Only this region on the forward tip of the nose cone has encountered the second mixture. Also, the pressure profile at the tube wall indicates a slight pressure reduction coincident with the pressure wave.

The pressure wave continues to travel toward the projectile base, and merges with the existing shock system, as illustrated in the pressure contours in both Fig. 21 and Fig. 22. The corresponding pressure profiles at the tube wall reveal reduced pressures in the regions where the wave has passed. As the wave encounters the conical shock reflecting from the tube wall, its presence is no longer visually apparent in the pressure contours, as evidenced in Fig. 23 through Fig. 25. Its effects are noticeable, however, in the corresponding pressure profiles. The amplitude of the pressure rise associated with the initial conical shock as well as the peak pressure value decrease by approximately 20%.

The interaction between the oblique shocks generated by the projectile and the mixture interface depends heavily on the acoustic impedance of the two gas mixtures [29,30,31]. The acoustic impedance, z, is defined as the product of the fluid density and the sound speed, $z=\rho c$. The relationship between the acoustic impedances of the gas mixtures on either side of the interface determines the wave behavior at the interface. An increase in acoustic impedance results in the reflection of a shock from the boundary back into the first mixture, while a decrease results in the propagation of an expansion wave back into the first mixture. Matching values at the contact

surface prevent any shock reflection or expansion, effectively removing the influence of the boundary.

In this constant Mach number transition, the acoustic impedances of the first and second mixtures are 11,040 Rayl and 8180 Rayl, respectively, (1 Rayl = 1 kg/m^2/sec). Consequently, as the projectile travels from the first mixture into the second, an expansion wave propagates back on to the projectile. The low pressure wave travelling over the projectile captured by the numerical simulation represents this propagating expansion wave.

Figure 26 shows the projectile upon completion of the transition process. The pressure contours reveal the newly stabilized shock structure after transition which, in this case, closely resembles the shock structure prior to transition. It should be noted that the shock structure is determined by the projectile Mach number [32,33]. Since the Mach number remains constant, the shock structure after transition is identical to the shock structure prior to transition, as previously displayed in Fig. 19. Also, since the shock structure does not change, the pressure ratio across the shocks does not change. Therefore, the pressure throughout the flow field is uniformly reduced, as illustrated by the pressure profile at the tube wall.

The constant Mach number transition discussed above has also been investigated experimentally with the densely instrumented ram accelerator section. Figure 27 reveals the experimental pressure profile at the tube wall prior to transition. The pressure profile shows both the initial conical shock and the first shock reflection from the projectile body, again represented by the initial pressure rise and the first sharp pressure peak, respectively. The

experimental pressure profile also exhibits a normal shock behind the first shock reflection, denoted by a sharp pressure rise. (The numerical model currently does not include this normal shock.)

Figure 28 contains the pressure profiles at the tube wall obtained from pressure transducers placed at the first four stations in the densely instrumented ram accelerator section. Figure 29 contains pressure profiles obtained from the remaining four stations. The pressure traces are arranged chronologically with the earliest trace at the bottom of the graph. The pressure profiles are all qualitatively similar to each other, as expected. It is not obvious, however, that the absolute pressure magnitudes decrease during the transition process since three dimensional effects make comparisons between pressure traces ambiguous [13].

Figure 30 shows the pressure at the tube wall upon completion of the transition process. Again, as anticipated, the qualitative trends of this pressure trace are similar to those displayed prior to transition in Fig. 27. The initial conical shock, its first reflection, and a distinct normal shock are all evident, but a comparison between pressure amplitudes is not made.

CASE 2: CONSTANT PRESSURE TRANSITION

The projectile in the second experiment makes a transition from the nominal ram accelerator first stage mixture to the nominal second stage mixture. These mixtures have different densities and sound speeds, and consequently the projectile Mach number varies between the mixtures, as well. The pressure between mixtures, however, remains constant.

Figure 31 shows the pressure contours and pressure profiles at the wall determined computationally for a point prior to the transition. The pressure contours reveal a well established oblique shock system along the projectile. As before, the first pressure rise in the wall pressure profile corresponds to the initial conical shock, while the pressure peak corresponds to the first reflection from the projectile body.

Figure 32 depicts the first contact between the projectile and the second gas mixture. The pressure contours indicate that the conical shock system remains unchanged, except in the forward region, where a disturbance has propagated on to the projectile nose cone. Only this region on the forward tip of the nose cone has encountered the second mixture. Also, although the pressure profile at the tube wall indicates the presence of a disturbance, the pressure reduction observed during the constant Mach number transition is not present. Examination of the density contours reveals that the propagating disturbance in the constant pressure transition coincides with a density interface. Therefore, this disturbance represents the contact surface passing over the projectile. It should be noted that there is no pressure change across the contact surface; the distinguishing mark indicating the contact surface in the pressure profiles is simply a computational artifact.

In the constant Mach number transition, an expansion wave resulting from the lower acoustic impedance of the second stage mixture was observed. In the constant pressure transition, however, the acoustic impedances of the first and second stages are 9220 Rayl and 7050 Rayl, respectively. The

decrease in acoustic impedances between mixtures during this constant pressure transition is not as drastic as the decrease during the constant Mach number transition. Consequently, the expansion wave propagating back on to the projectile in the constant pressure transition is not as strong as the expansion wave captured in the constant Mach number transition. This weaker expansion wave is not visible in the numerical simulation of the constant pressure transition.

The contact surface continues to travel toward the projectile base, distorting the initial conical shock, as illustrated by the pressure contours in Fig. 33 and Fig. 34. The corresponding pressure profiles at the tube wall also show the propagating disturbance. As the contact surface encounters the conical shock reflection at the tube wall, it becomes evident that the conical shock angle (measured from the horizontal) has been increased, as shown in Fig. 35. The associated wall pressure profile also begins to change shape. In Fig. 36 and Fig. 37, the contact surface interacts with the next two reflected shocks causing them to move forward on to the projectile nose cone, and the pressure profiles continue to change.

Figure 38 depicts the projectile upon completion of the transition process. The pressure contours show that the newly stabilized shock structure is very different from the original structure presented in Fig. 31. This effect is consistent with aerodynamic theory. Since the projectile enters a mixture with a higher sound speed, the Mach number decreases. Consequently, the oblique shock moves forward, allowing the shock to undergo an additional reflection before expanding over the projectile

shoulder, as shown by the pressure contours. The additional reflection compresses the gas mixture even further, creating a higher peak pressure in the wall pressure profile. The forward motion of the shock also creates a larger time interval between the first indications of the conical shock and the peak pressure.

The constant pressure transition discussed above occurs in almost every experiment since it utilizes the nominal first and second stage mixtures. Therefore, it is an ideal candidate for study with the densely instrumented ram accelerator section. Figure 39 reveals the wall pressure profile prior to transition. The pressure profile clearly indicates the conical shock, its first reflection, and the normal shock.

Figures 40 and 41 contain the pressure profiles obtained from the stations in the densely instrumented ram accelerator section. Each graph presents the pressure traces in chronological order with the earliest trace at the bottom. Although it is difficult to draw quantitative conclusions, the time increment between the conical shock and the pressure peak associated with the its first reflection does appear to increase. The motion of the normal shock provides another interesting observation. As the projectile begins the transition, as depicted in the lowest trace in Fig. 40, the normal shock is distinct and separated from the oblique shock system. In the next three pressure traces, the normal shock is no longer separated from the oblique shock system, indicating that it has moved forward. The pressure traces in Fig. 41, however, again show a distinct normal shock, indicating that the normal shock has moved away from the oblique shock system. This motion of

the normal shock is currently not modeled numerically, but may play an important role in understanding the ram accelerator. Should the normal shock move forward too far, for instance, it could choke the flow at the projectile throat, resulting in a projectile unstart.

Finally, the pressure profile at the tube wall upon completion of the transition process appears in Fig. 42. This profile is very different from the profile prior to transition displayed in Fig. 39. Most notably, however, the final pressure profile indicates two distinct pressure peaks before the normal shock, suggesting two shock reflections, as opposed to the first profile which only shows one reflection. These data provide physical evidence of the changes in shock structure predicted by the numerical model.

Level	P (atm)
D	103.056
C	97.346
B	91.636
A	85.9261
9	80.2161
8	74.5061
7	68.7961
6	63.0862
5	57.3762
4	51.6662
3	45.9562
2	40.2463
1	34.5363

PRESSURE AT TUBE WALL (atm)

TIME (usec)

CONICAL SHOCK
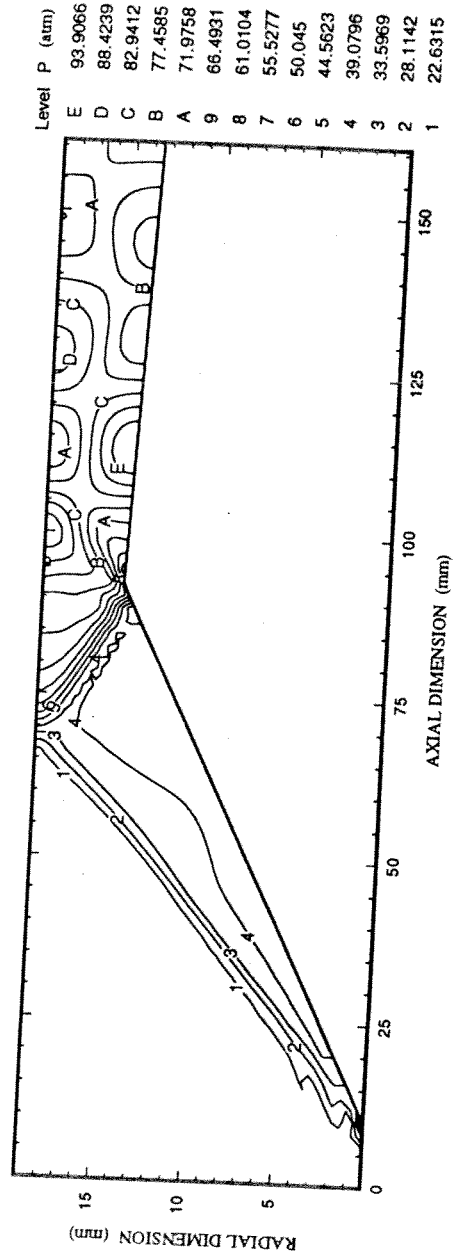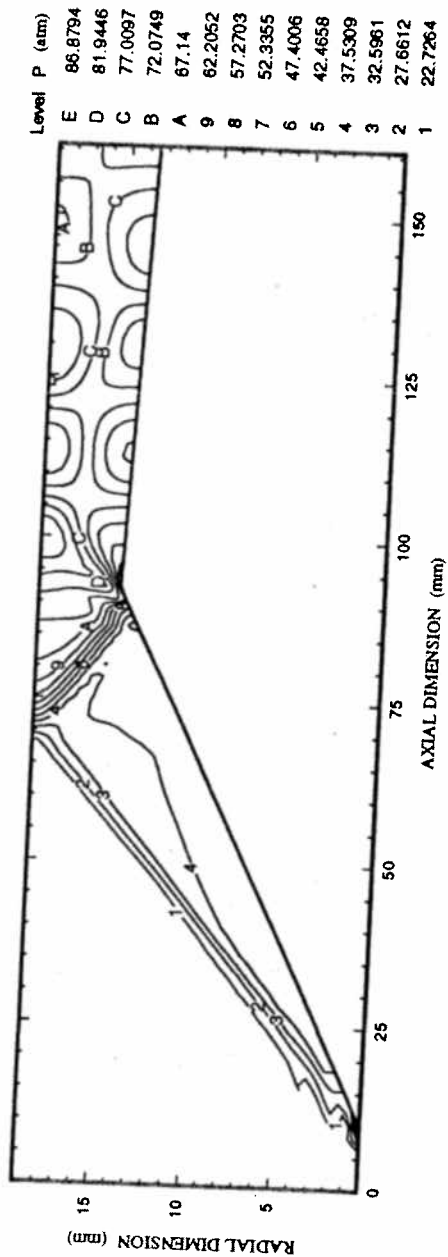
REFLECTION

AXIAL DIMENSION (mm)

RADIAL DIMENSION (mm)
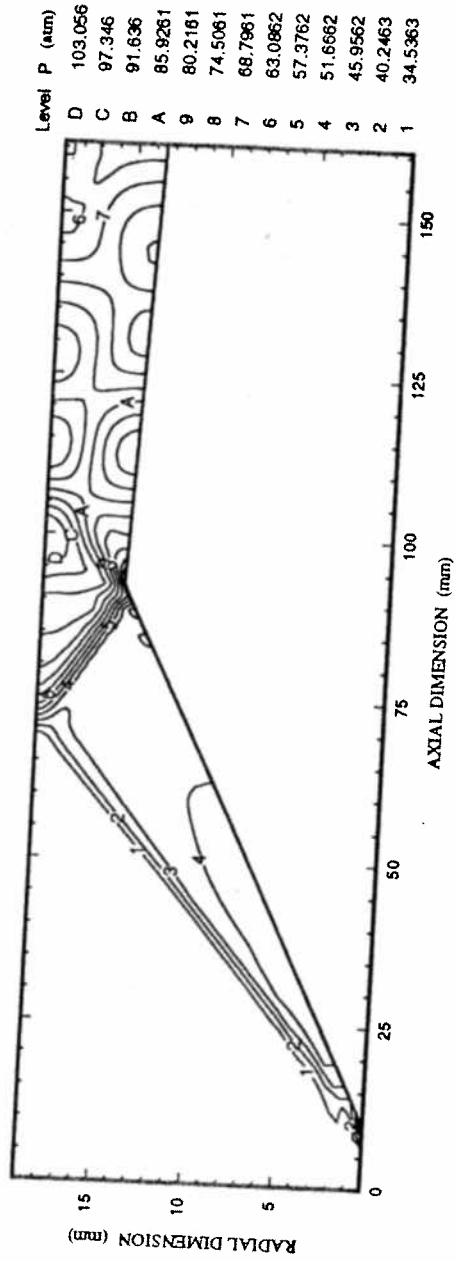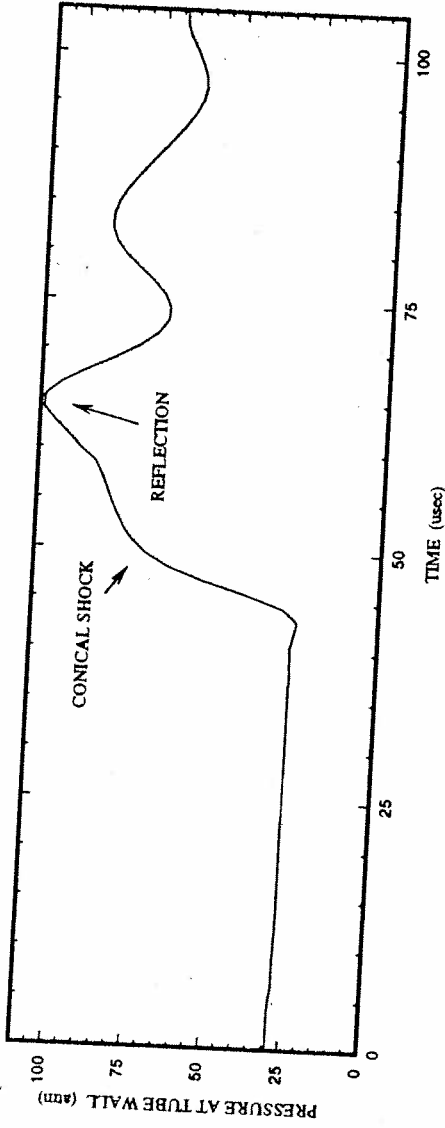
Fig. 19: Numerical Pressure Contours and Wall Pressure Profile
Prior to Constant Mach Number Transition.
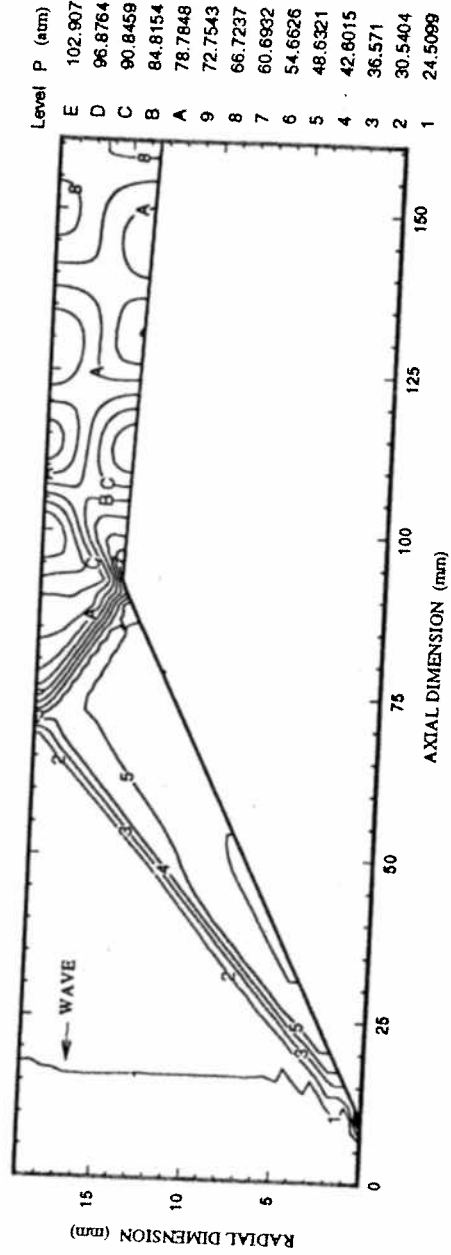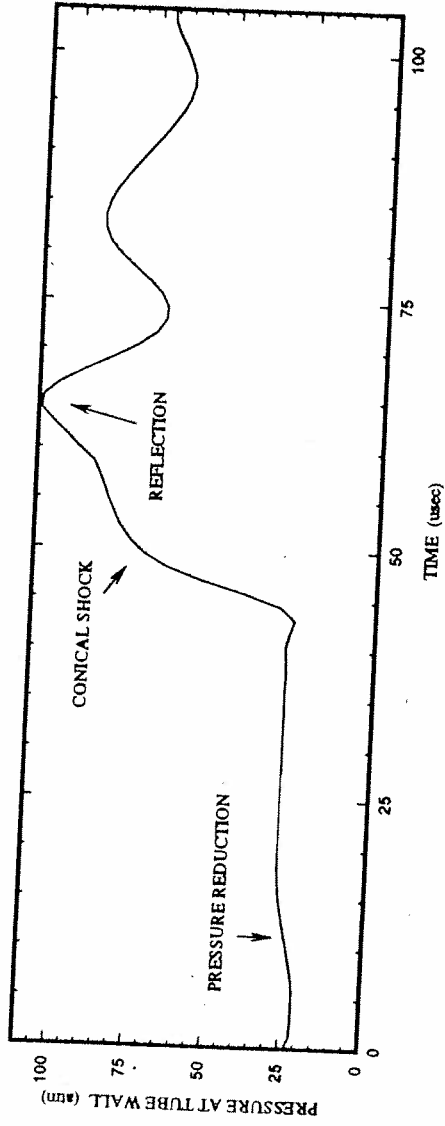
Fig. 20: Numerical Pressure Contours and Wall Pressure Profile During Constant Mach Number Transition. (x=20 mm)
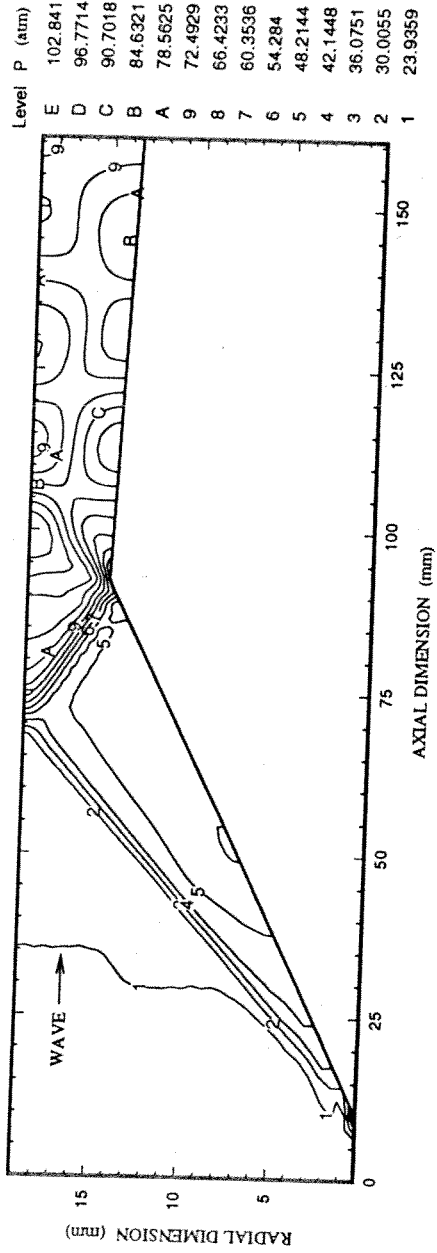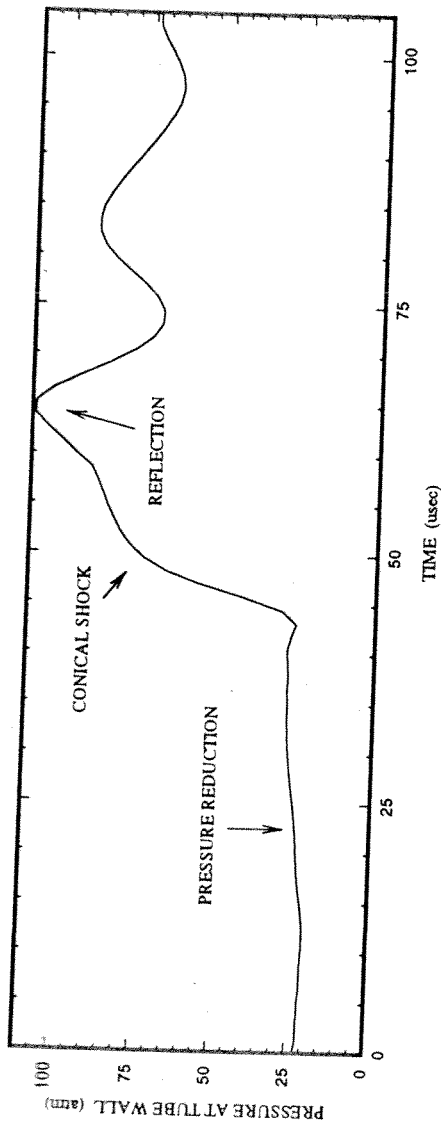
Fig. 21: Numerical Pressure Contours and Wall Pressure Profile
During Constant Mach Number Transition. (x=40 mm)
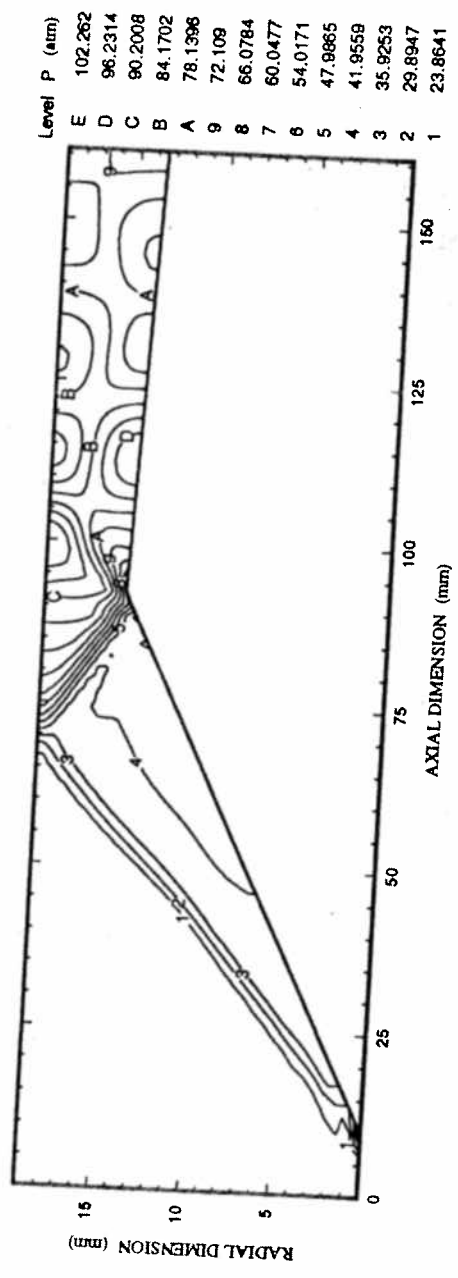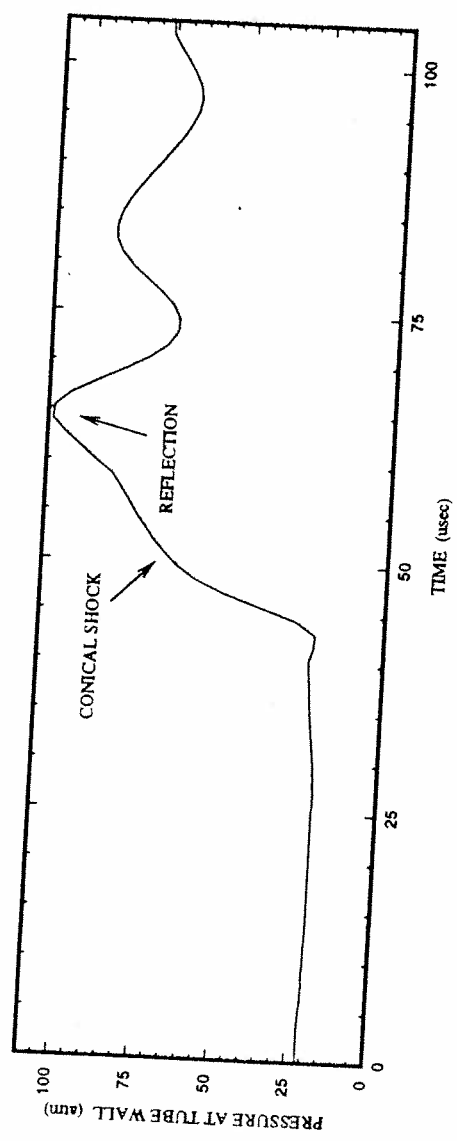
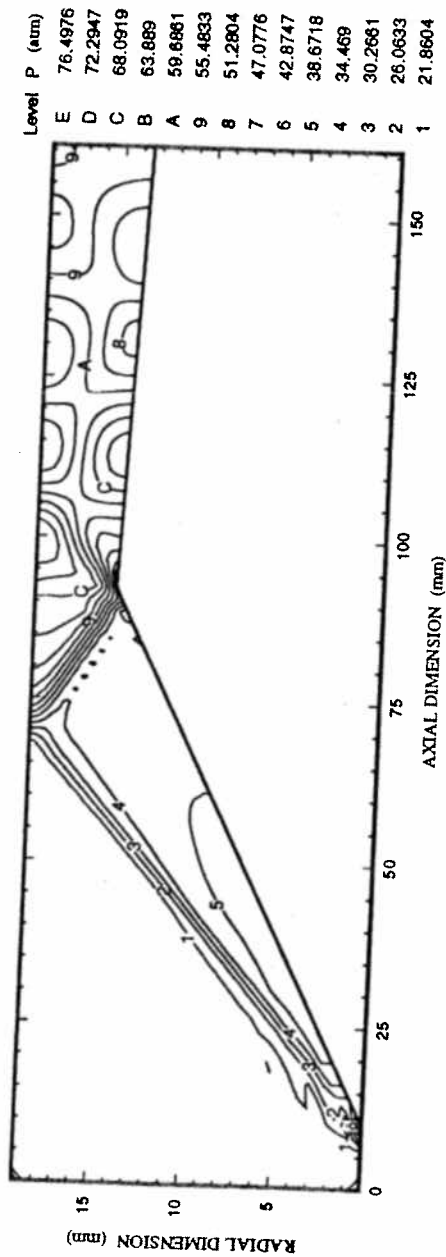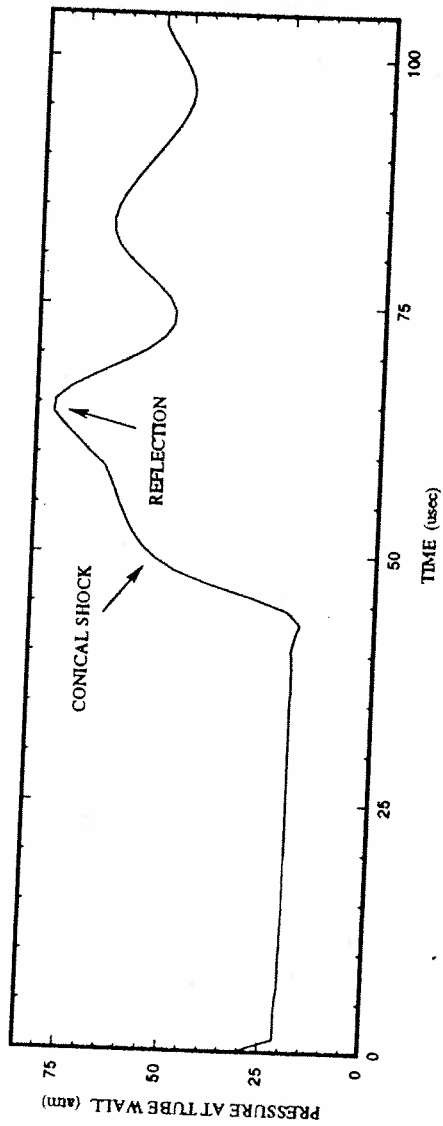Fig. 23: Numerical Pressure Contours and Wall Pressure Profile During Constant Mach Number Transition. (x=80 mm)
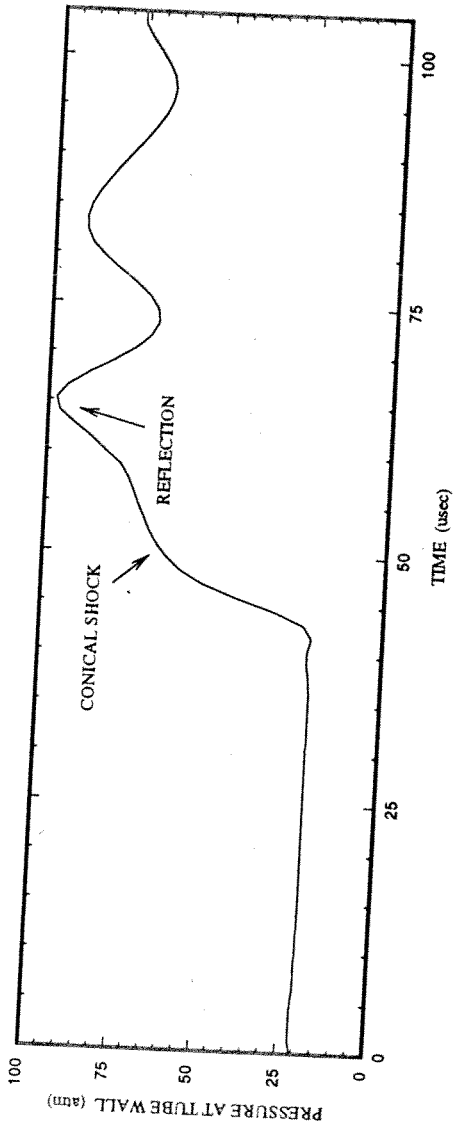
Fig. 24: Numerical Pressure Contours and Wall Pressure Profile
During Constant Mach Number Transition. (x=100 mm)
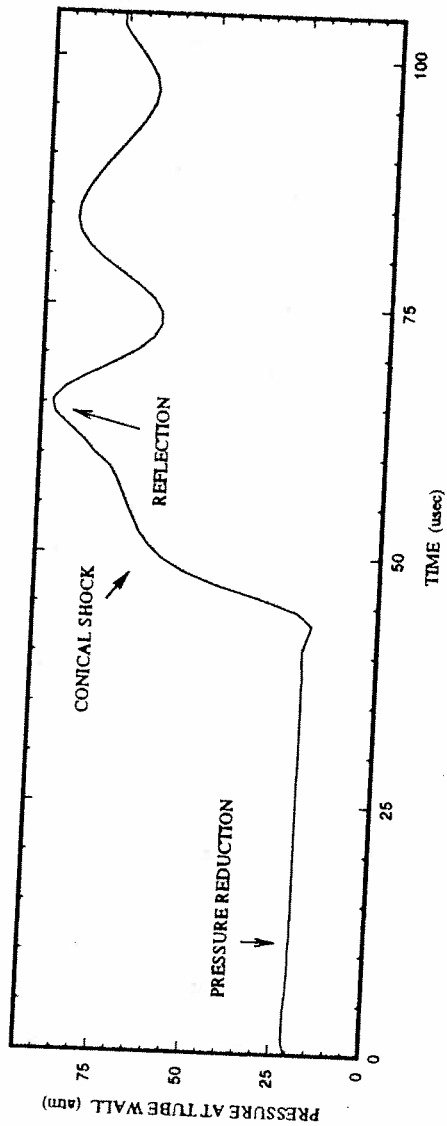
Fig. 25: Numerical Pressure Contours and Wall Pressure Profile During Constant Mach Number Transition. (x=120 mm)

Fig. 26: Numerical Pressure Contours and Wall Pressure Profile
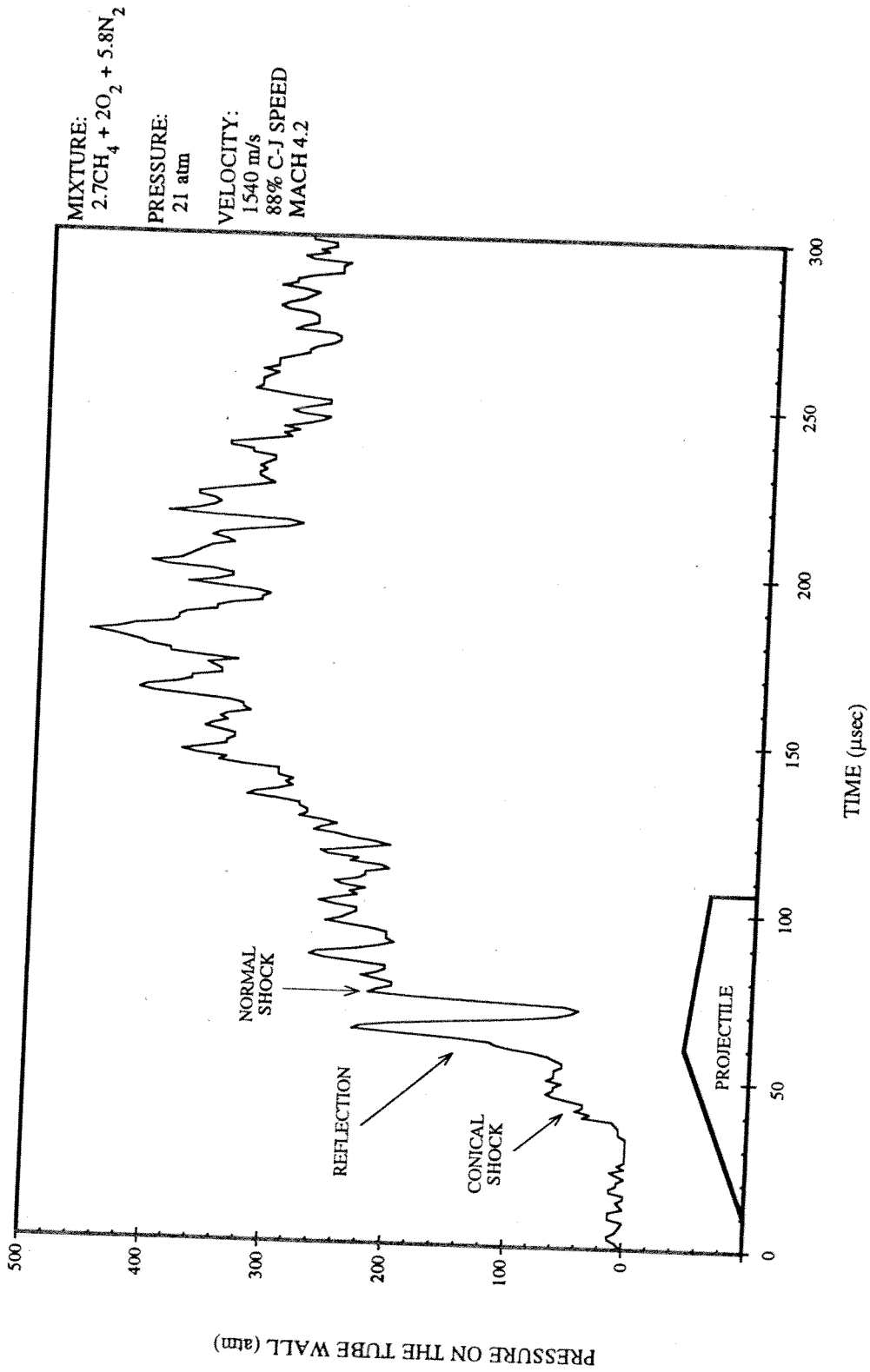Upon Completion of Constant Mach Number Transition.

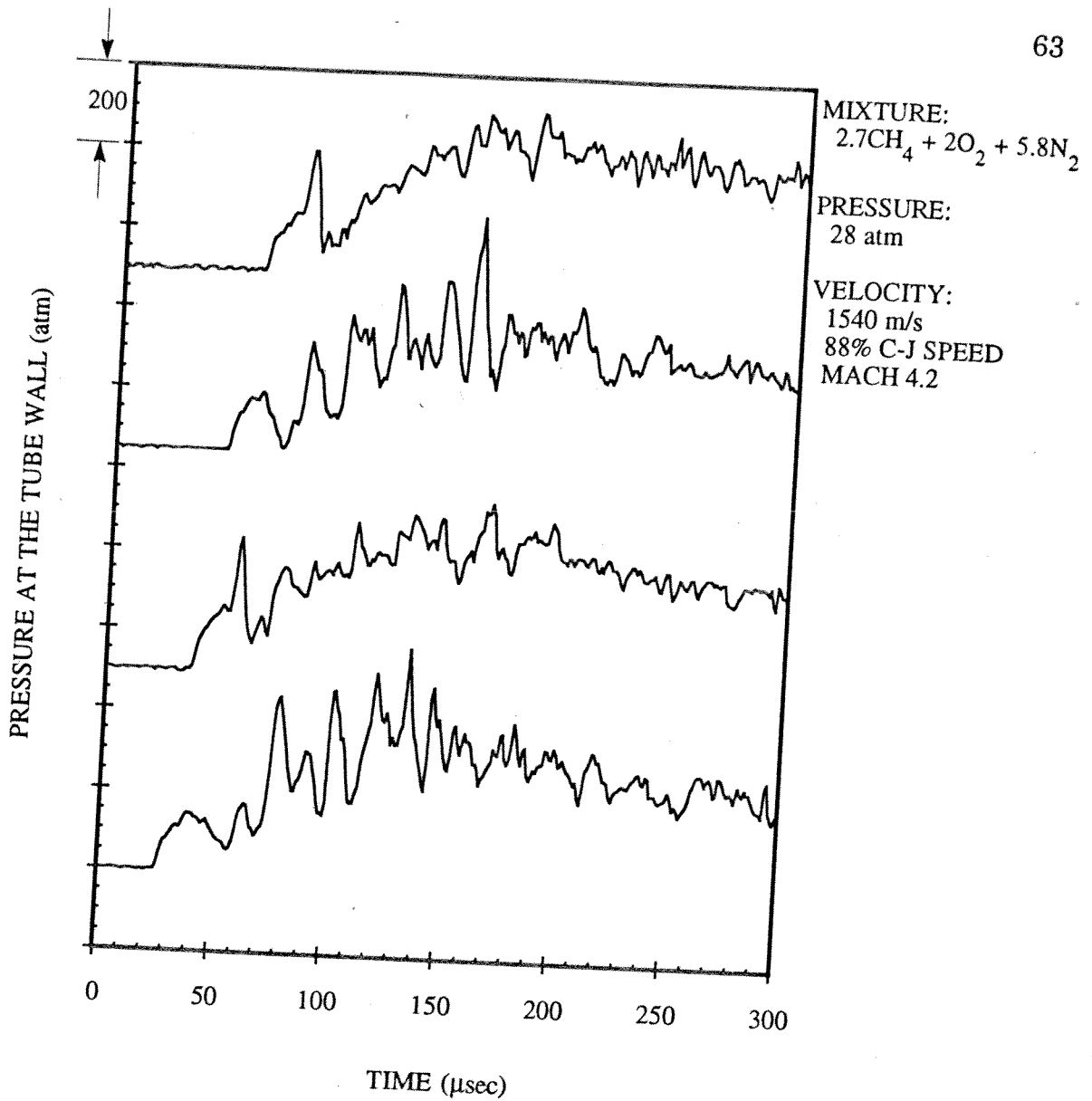Fig. 27: Experimental Wall Pressure Profile Prior to Constant Mach Number Transition.

Fig. 28: Experimental Wall Pressure Profiles from First Four Stations of Densely Instrumented Ram Accelerator Section During Constant Mach Number Transition.
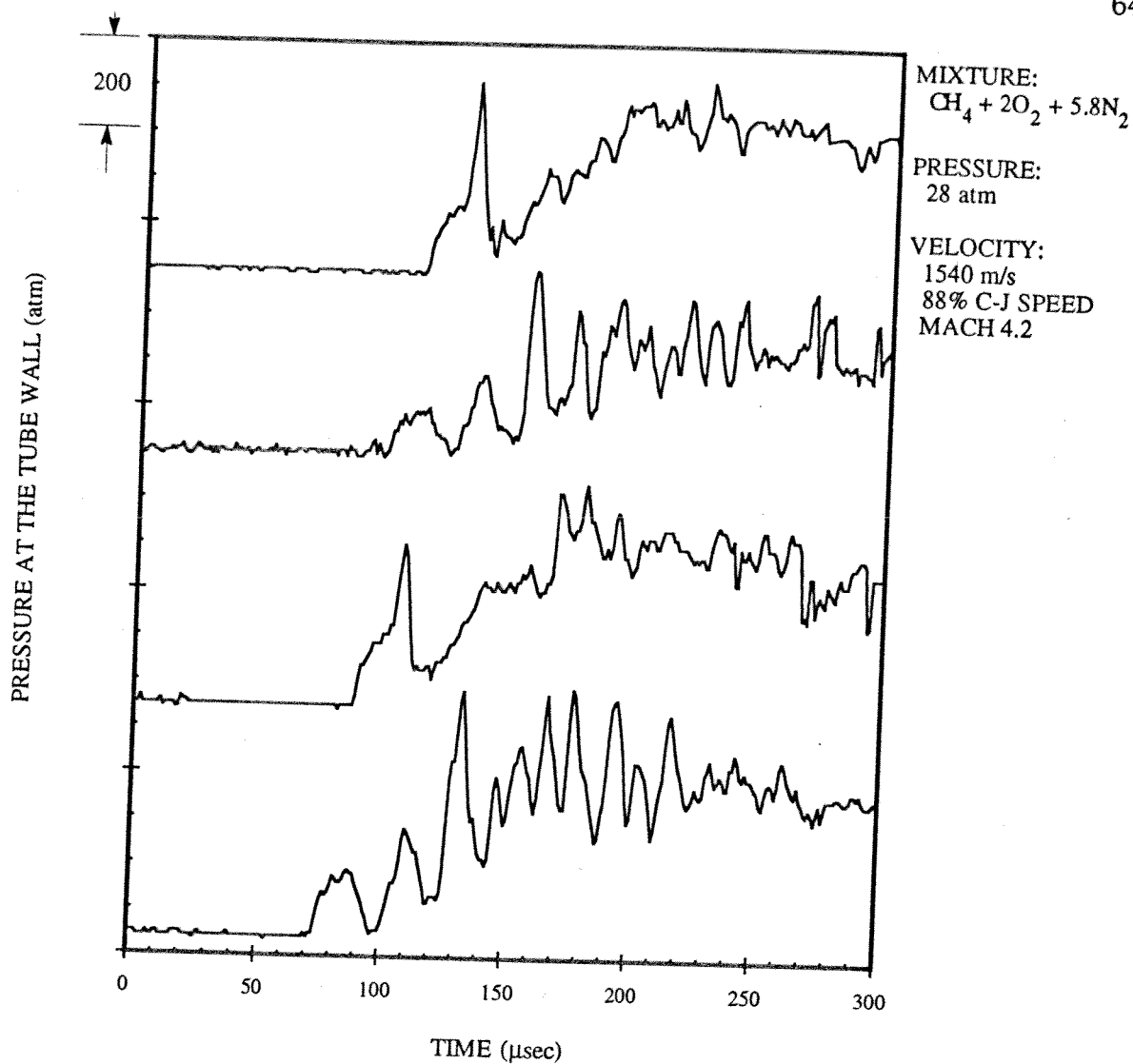
Fig. 29: Experimental Wall Pressure Profiles from Second Four Stations of Densely Instrumented Ram Accelerator Section During Constant Mach Number Transition.
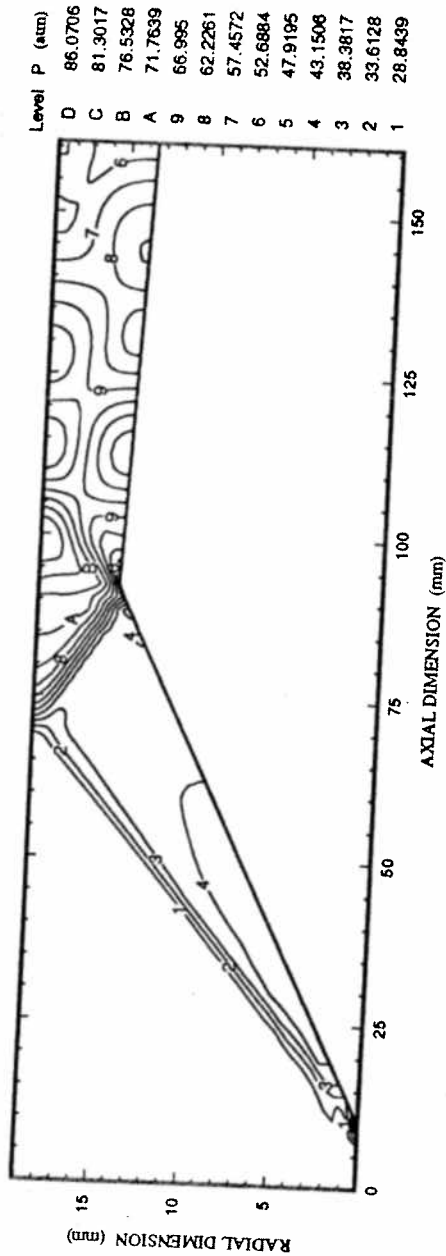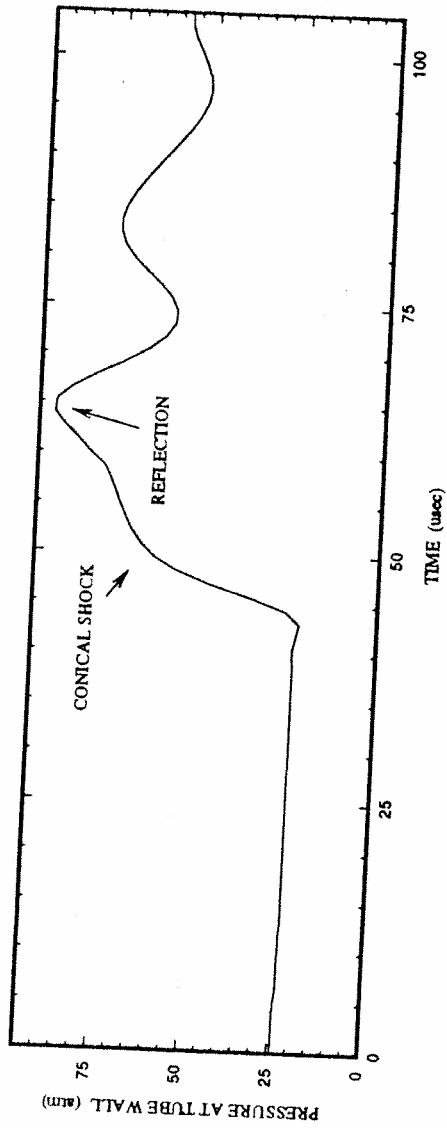
Fig. 31: Numerical Pressure Contours and Wall Pressure Profile Prior to Constant Pressure Transition.
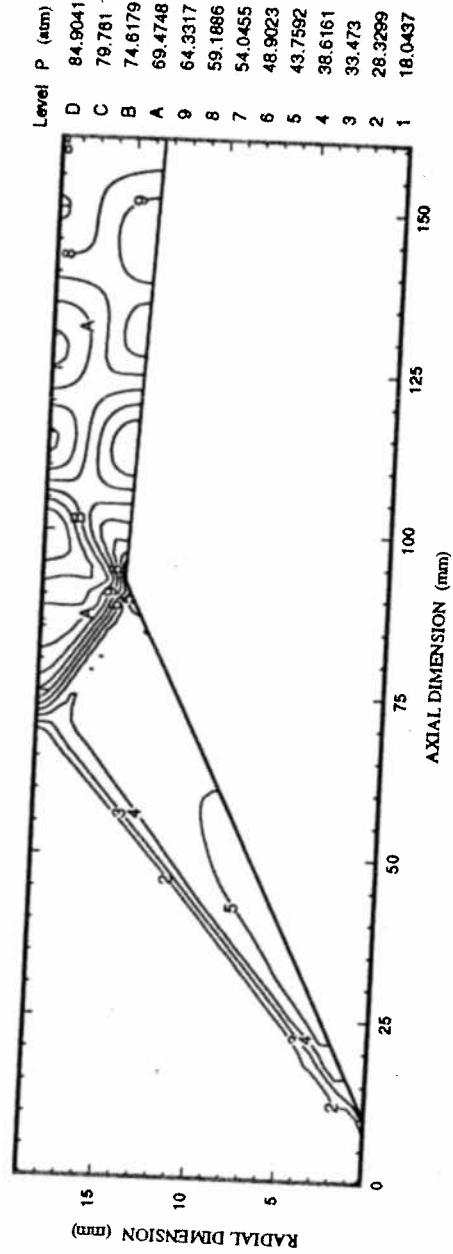
Fig. 32: Numerical Pressure Contours and Wall Pressure Profile
During Constant Pressure Transition. (x=20 mm)

Fig. 34: Numerical Pressure Contours and Wall Pressure Profile
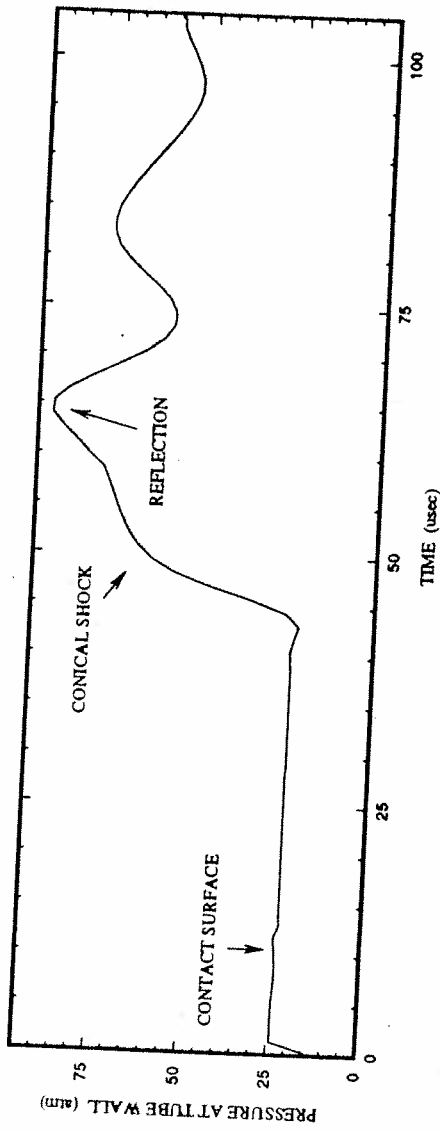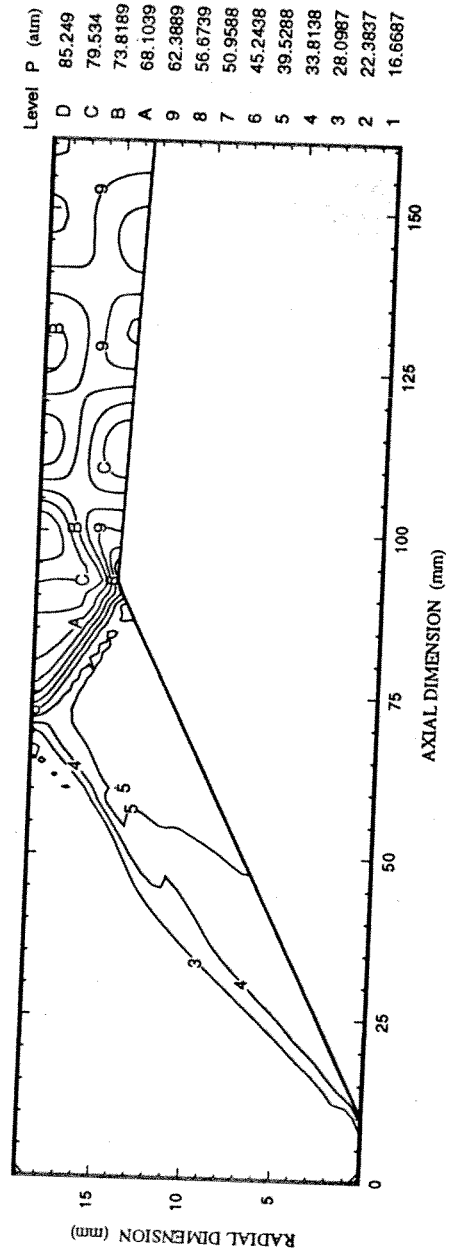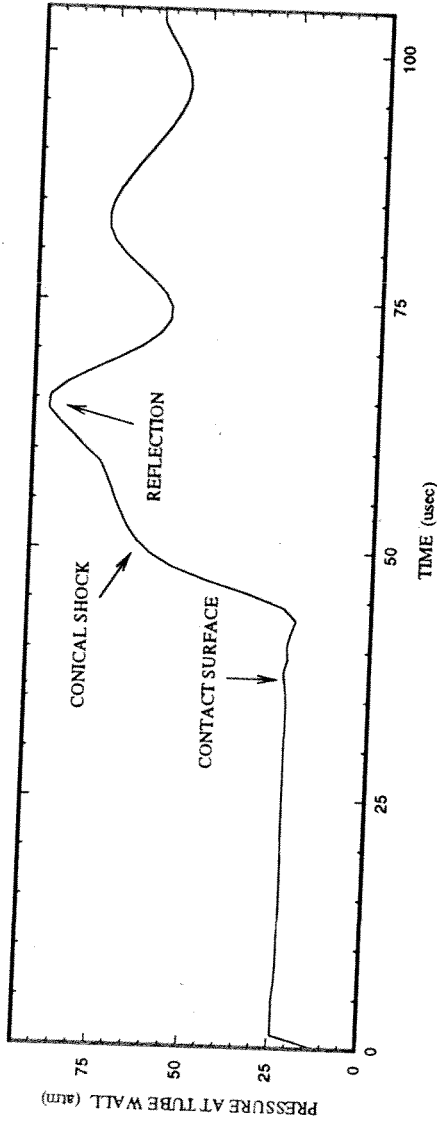During Constant Pressure Transition. (x=60 mm)

Fig. 35: Numerical Pressure Contours and Wall Pressure Profile
During Constant Pressure Transition. (x=80 mm)
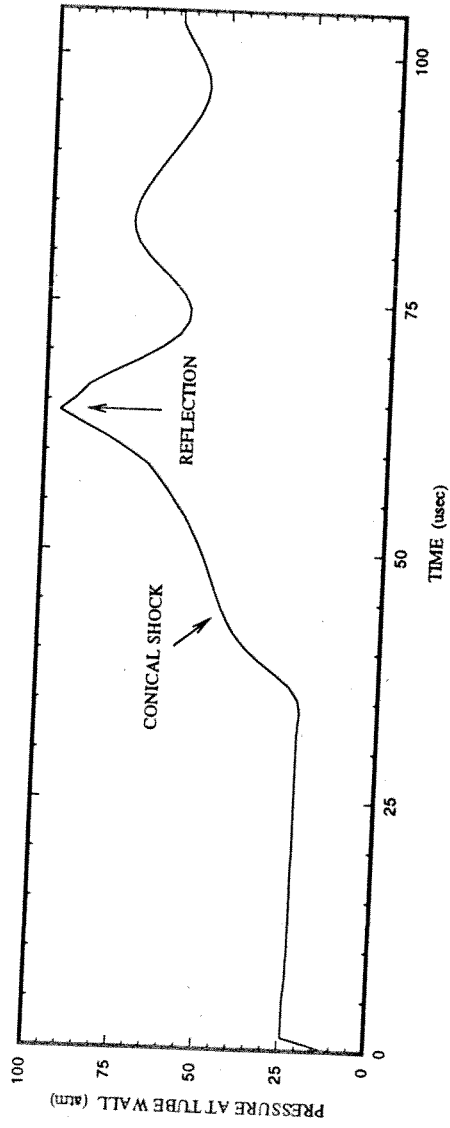
Fig. 36: Numerical Pressure Contours and Wall Pressure Profile
During Constant Pressure Transition. (x=100 mm)

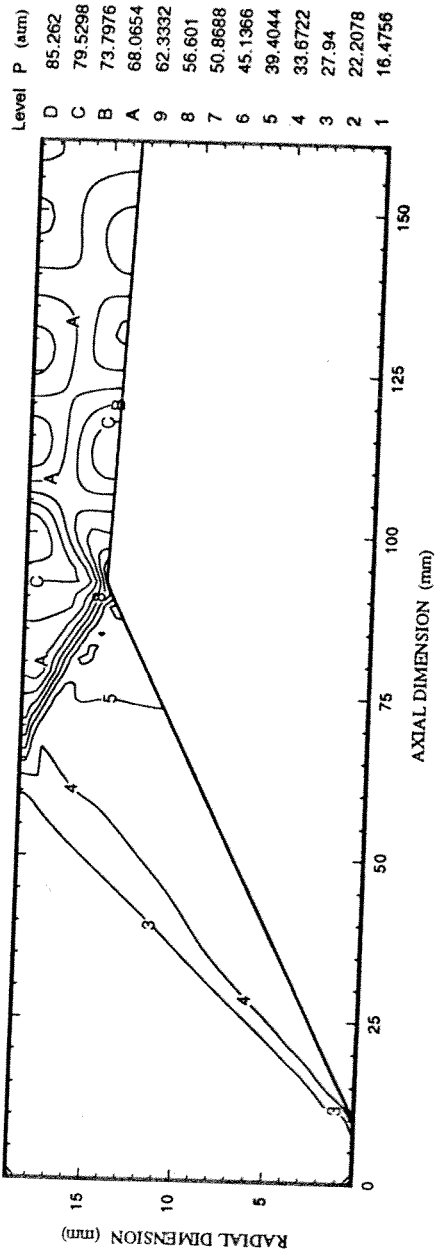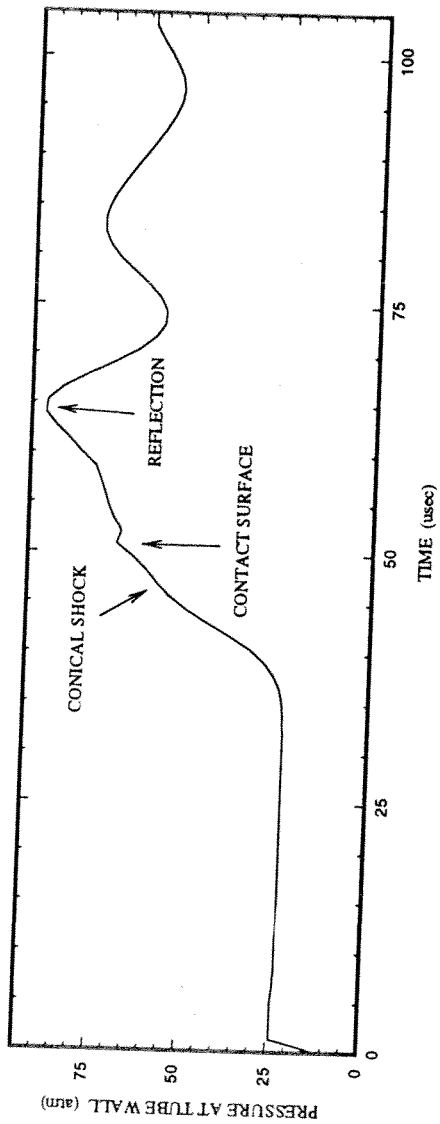| Level	P (atm)
D	89.7208
C	83.6107
B	77.5005
A	71.3904
9	65.2803
8	59.1702
7	53.0601
6	46.9499
5	40.8398
4	34.7297
3	28.6195
2	22.5094
1	16.3993

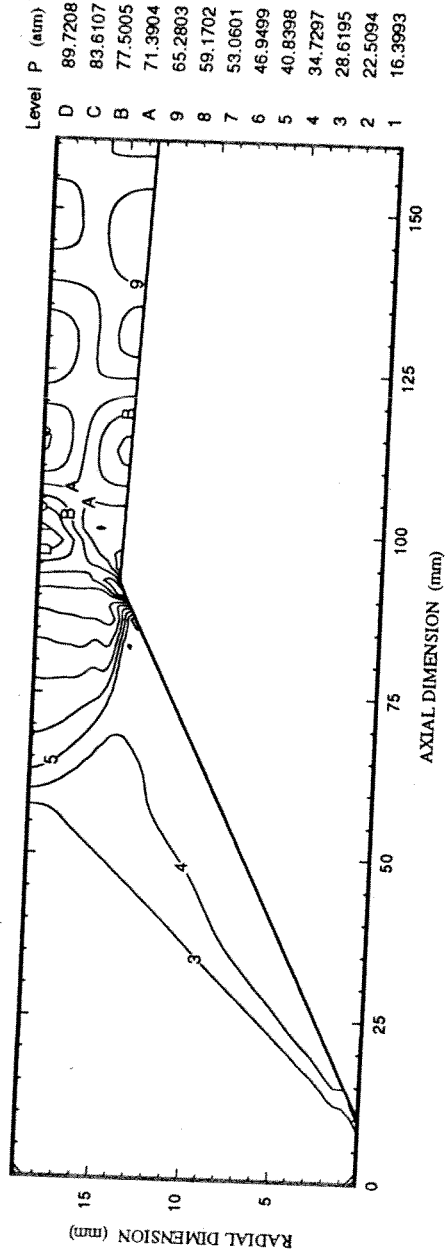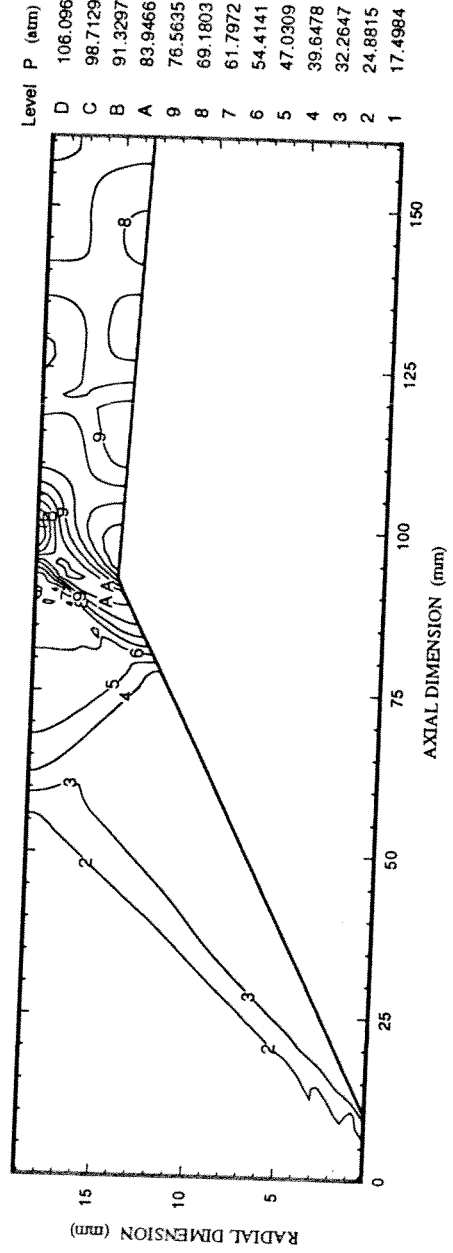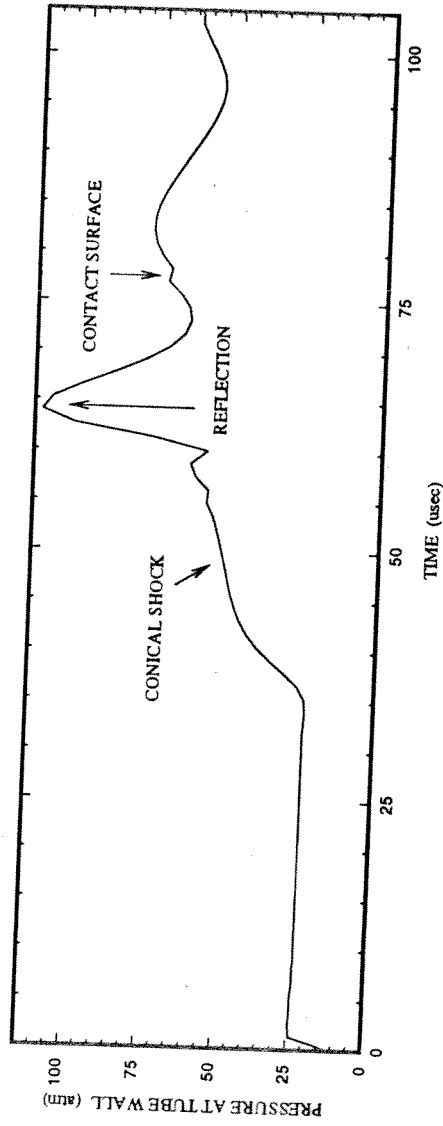Fig. 37: Numerical Pressure Contours and Wall Pressure Profile During Constant Pressure Transition. (x=120 mm)

Fig. 40: Experimental Wall Pressure Profiles from First Four Stations of Densely Instrumented Ram Accelerator Section During Constant Pressure Transition.

Fig. 41: Experimental Wall Pressure Profiles from Second Four Stations of Densely Instrumented Ram Accelerator Section During Constant Pressure Transition.

MIXTURE:
$4.9CH_4 + 2O_2 + 3.9He$

PRESSURE:
24 atm

VELOCITY:
1540 m/s
73% C-J SPEED
MACH 3.2

Fig. 42: Experimental Wall Pressure Profile Upon Completion of Constant Pressure Transition.

VII: CONCLUSION

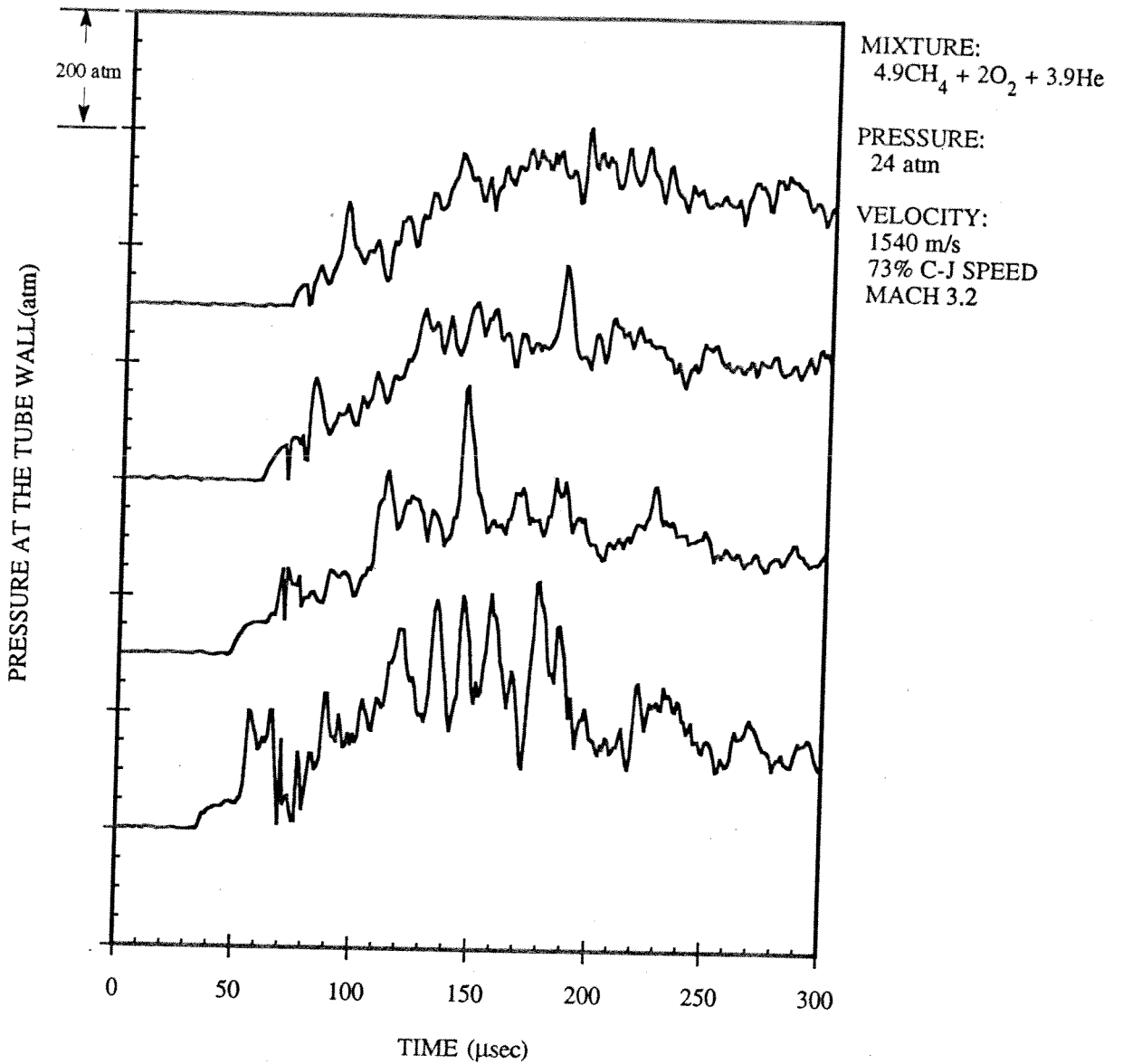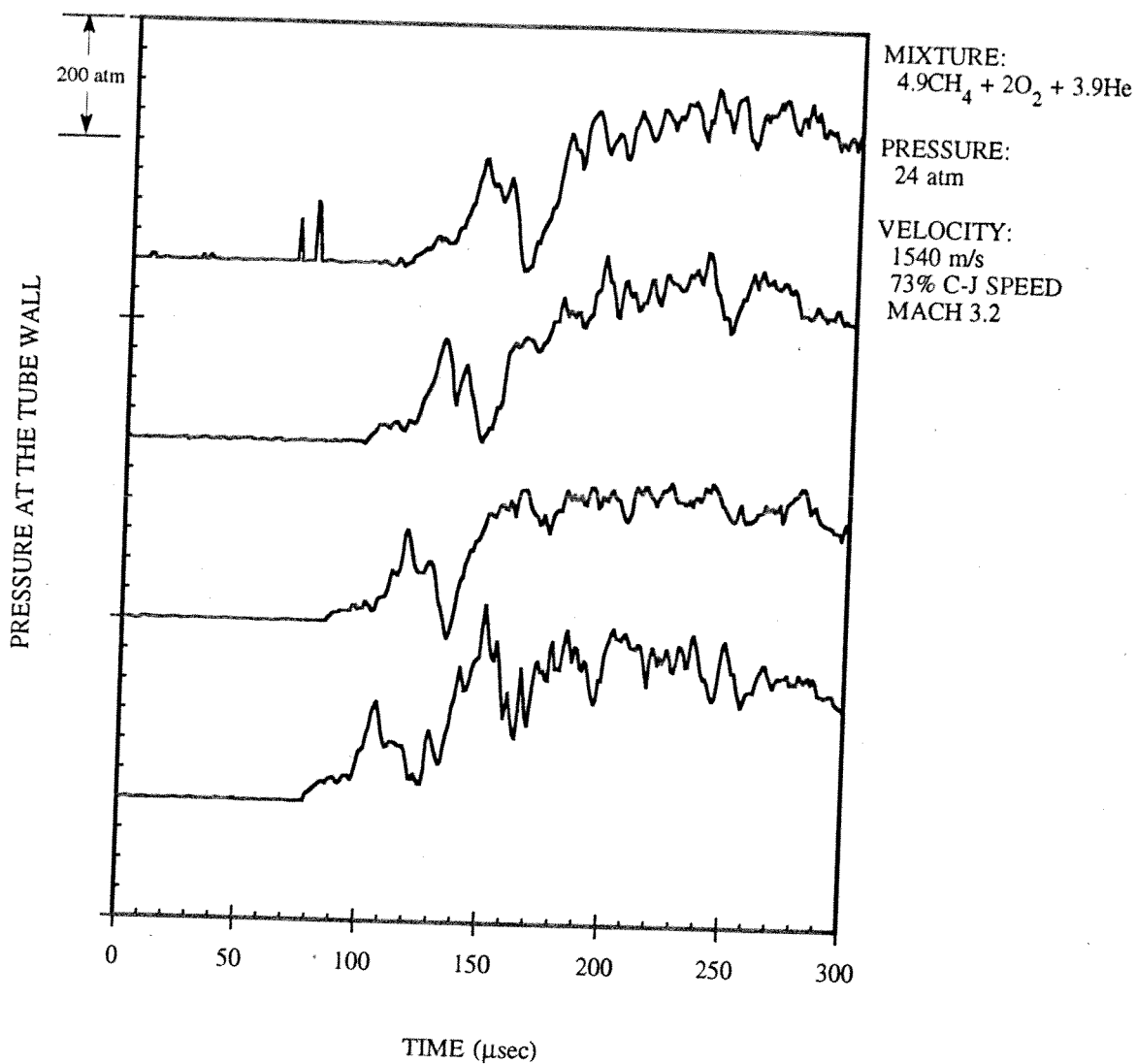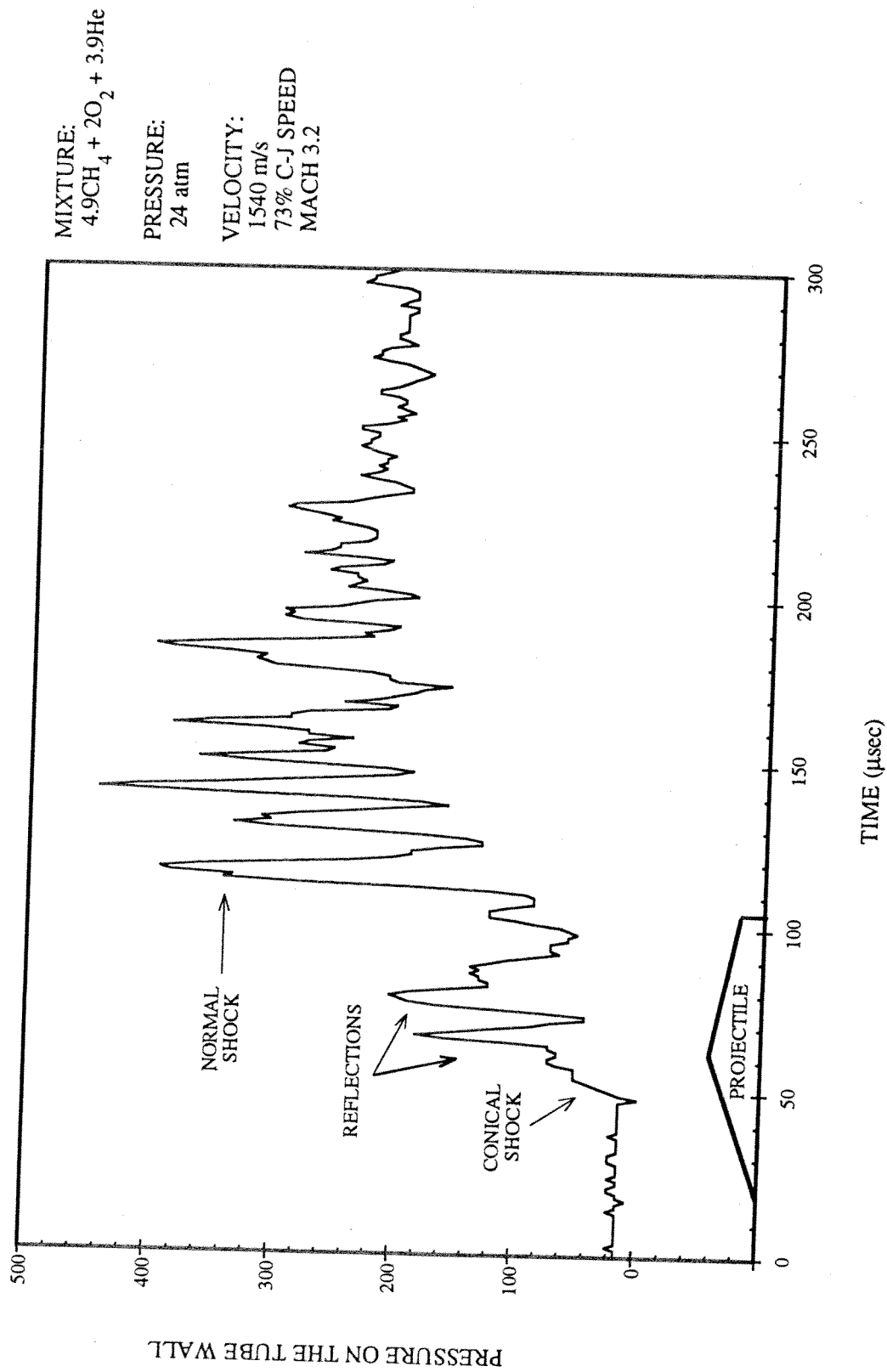This thesis has presented a numerical and experimental investigation of the ram accelerator mixture transition process. An axisymmetric MacCormack scheme was used to investigate the effects of mixture transition on the oblique shock structure about the projectile. The computational results were complemented by high resolution experimental data. Both a constant Mach number transition and a constant pressure transition were studied.

Calculations performed on the constant Mach number transition captured an expansion wave propagating over the projectile. Since the Mach number across the transition interface remained constant, the shock structure remained unchanged, but the pressure amplitudes decreased. These results agreed qualitatively with data obtained experimentally.

Calculations performed on the constant pressure transition captured the contact surface propagating over the projectile and the changing forms of the oblique shock structure. Again, the results agreed qualitatively with experimental data.

During the course of ram accelerator investigation, different mixture transitions may provide different advantages. The constant Mach number transition, for instance minimizes wave motion and other unsteady effects, effectively providing a more stable and reliable transition. The pressure ratios across the transition interface required to create the constant Mach number transition, however, may be prohibitively large.

The constant pressure transition avoids any difficulties incurred with high pressure differences, but also results in a more unstable transition due to excessive wave motion. Matching the acoustic impedances of the mixtures may provide the most attractive transition since the effect of the boundary would be removed entirely, resulting in the most stable configuration.

Transition studies could be further enhanced by modifying the axisymmetric model presented here to include heat addition effects. A transparent tube section could also provide visual data to enhance understanding of the physical processes. By gaining a greater understanding the ram accelerator transition process, more reliable ram accelerator performance can be achieved.

REFERENCES

[1]   Hertzberg, A., Bruckner, A. P., and Bogdanoff, D. W., "Ram Accelerator: A New Chemical Method for Accelerating Projectiles to Ultrahigh Velocities," _AIAA Journal_, vol. 26, no. 2, February, 1988, pp. 195-203.

[2]   Hertzberg, A., Bruckner, A. P., Bogdanoff, D. W., Knowlen, C., "The Ram Accelerator and its Applications: A New Approach for Reaching Ultrahigh Velocities," _Proceedings of the 16th International Symposium on Shock Tubes and Waves_, Aachen, West Germany, July 26-30, 1987, pp. 117-128.

[3]   Bruckner, A. P., Hertzberg, A., and Knowlen, C., "Review of Ram Accelerator Propulsion Modes," _27th JANNAF Combustion Subcommittee Meeting_, Warren AFB, Cheyenne, WY, November 5-9, 1990.

[4]   Kaloupis, P. and Bruckner, A. P., "The Ram Accelerator: A Chemically Driven Mass Launcher," AIAA Paper 88-2968, AIAA/ASME/SAE/ASEE 24th Joint Propulsion Conference, Boston, MA, July 11-13, 1988.

[5]   Bruckner, A. P., and Hertzberg, A., "Ram Accelerator Direct Launch System for Space Cargo," IAF Paper 87-211, 38th Congress of the International Astronautical Federation, Brighton, United Kingdom, October 10-17, 1987.

[6]   Hertzberg, A., Bruckner, A. P., and Knowlen, C., "The Ram Accelerator as a Hypersonic Test Facility," 16th Aerodynamic Ground Testing Conference, Seattle, WA, June 18-20, 1990.

[7]   Bruckner, A. P., Chew, G., Auzias de Turenne, J., and Dunmire, B., "Investigation of Hypersonic Ramjet Propulsion Cycles Using a Ram Accelerator Test Facility," 42nd Congress of the International Astronautical Federation, Montreal, Canada, October 5-11, 1991.

[8]   Chew, G., Knowlen, C., Burnham, E. A., Hertzberg, A., Bruckner, A. P., "Experiments on Hypersonic Ramjet Propulsion Cycles Using a Ram Accelerator," AIAA Paper 91-2489, 27th AIAA/SAE/ASME Joint Propulsion Conference, Sacramento, CA, June 24-26, 1991.

[9]   Knowlen, C., Bruckner, A. P., Bogdanoff, D. W., and Hertzberg, A., "Performance Capabilities of the Ram Accelerator," AIAA Paper 87-2152, AIAA/SAE/ASME/ASEE 23rd Joint Propulsion Conference, San Diego, CA, June 29-July 2, 1987.

81

[10] Christofferson, E., <u>A Magnetic Transducer Detection System for High Speed Projectiles in Tubes</u>, M.S.A.A. Thesis, Department of Aeronautics and Astronautics, University of Washington, Seattle, WA, December, 1989.

[11] Prochko, A., <u>Preliminary Spectral Analysis of the Ram Accelerator</u>, M.S.A.A. Thesis, Department of Aeronautics and Astronautics, University of Washington, Seattle, WA, March, 1991.

[12] McIntosh, R., <u>A Microsecond Response Thermocouple in the Ram Accelerator</u>, M.S.A.A. Thesis, Department of Aeronautics and Astronautics, University of Washington, Seattle, WA, March, 1991.

[13] Hinkey, J. H., Burnham, E. A., and Bruckner, A. P., "High Spatial Resolution Measurements of Ram Accelerator Gas Dynamic Phenomena," AIAA Paper 92-3244, AIAA/SAE/ASME/ASEE 28th Joint Propulsion Conference, Nashville, TN, July 6-8, 1992.

[14] Burnham, E. A., <u>Experimental and Numerical Analysis of the Thermally Choked Ram Accelerator Starting Process</u>, M.S.A.A. Thesis, Department of Aeronautics and Astronautics, University of Washington, Seattle, WA, 1989.

[15] Bruckner, A. P., Burnham, E. A., Knowlen, C., Hertzberg, A., and Bogdanoff, D. W., "Initiation of Combustion in the Thermally Choked Ram Accelerator," 18th International Symposium on Shock Waves, Sendai, Japan, July 21-26, 1991.

[16] Bruckner, A. P., Knowlen, C., Hertzberg, A., and Bogdanoff, D. W., "Operational Characteristics of the Thermally Choked Ram Accelerator," <u>Journal of Propulsion and Power</u>, vol. 7, no. 5, September-October, 1991, pp. 828-836.

[17] Knowlen, C., Scott, K. A., Bruckner, A. P., and Hertzberg, A., "Recent Developments in Ram Accelerator Technology," <u>39th Meeting of the Aeroballistics Range Association</u>, Albuquerque, NM, October 10-13, 1988.

[18] Kaloupis, P., <u>An Unsteady Total Variational Diminishing Axisymmetric Numerical Model for the Ram Accelerator Subsonic Combustion Thermal Choking Propulsion Mode</u>, M.E.A.A. Thesis, Department of Aeronautics and Astronautics, University of Washington, Seattle, WA, 1990.

[19] Dunmire, B., <u>An Experimental and Theoretical Investigation of Single Stage Ram Accelerator Performance with Emphasis Towards Projectile Material Effects</u>, M.S.A.A. Thesis, Department of Aeronautics and Astronautics, University of Washington, Seattle, WA, September, 1991.

[20] Burnham, E. A., Kull, A. E., Knowlen, C., Bruckner, A. P., and Hertzberg, A., "Operation of the Ram Accelerator in the Transdetonative Velocity Regime," AIAA/SAE/ASME/ASEE 26th Joint Propulsion Conference, Orlando, FL, July 16-18, 1990.

[21] Knowlen, C., Burnham, E. A., Kull, A. E., Bruckner, A. P., and Hertzberg, A., "Ram Accelerator Performance in the Transdetonative Velocity Regime," 41st Meeting of the Aeroballistic Range Association, San Diego, CA, October 22-25, 1990.

[22] Kull, A. E., Burnham, E. A., Knowlen, C., Bruckner, A. P., and Hertzberg, A., "Experimental Studies of Superdetonative Ram Accelerator Modes," AIAA/ASME/SAE/ASEE 25th Joint Propulsion Conference, Monterey, CA, July 10-12, 1989.

[23] Ostrander, M. J., Hyde, M. F., Young, R. D., and Kissinger, R. D., "Standing Oblique Detonation Wave Engine Performance," AIAA Paper 87-2002, 1987.

[24] Yungster, S., Eberhardt, S., and Bruckner, A. P., "Numerical Simulation of Hypervelocity Projectiles in Detonable Gases," AIAA Journal, vol. 29, no. 2, February, 1991, pp. 187-199.

[25] MacCormack, R. W., "A Numerical Method for Solving the Equations of Compressible Viscous Flow," AIAA 19th Aerospace Sciences Meeting, AIAA Paper 81-0110, St. Louis, Missouri, January 12-15, 1981.

[26] Anderson, D. A., Tannehill, J. C., Pletcher, R. H., Computational Fluid Mechanics and Heat Transfer, Hemisphere Publishing Corporation, NY, 1984.

[27] Pulliam, T. H., "Artificial Dissipation Models for the Euler Equations," AIAA Journal, vol. 24, no. 12, December, 1986, pp. 1931-1940.

[28] Eberhardt, S., AA510 class notes, Department of Aeronautics and Astronautics, University of Washington, Spring quarter, 1991.

[29] Rudinger, G., Nonsteady Duct Flow, Dover Publications, Inc., NY, 1969.

[30] Meyers, R. A., editor, Encyclopedia of Physical Science and Technology, Academic Press, Inc., Vol. 1, 1987, Orlando, Fl.

[31] Parker, S. P., editor in chief, McGraw Hill, Encyclopedia of Science and Technology, 7th Edition, McGraw Hill, NY, 1992.

[32] Liepmann, H. W., Roshko, A., Elements of Gasdynamics, John Wiley & Sons, NY, 1957.

[33] Shapiro, A. H., <u>The Dynamics and Thermodynamics of Compressible Fluid Flows</u>, Vol. I, John Wiley & Sons, NY, 1953.